JOURNAL OF SPACECRAFT AND ROCKETS
Vol. 36, No. 3, May–June 1999

Aerothermodynamics of the Stardust Sample Return Capsule

David Olynick,* Y.-K. Chen,† and Michael E. Tauber‡
NASA Ames Research Center, Moffett Field, California 94035-1000

The development of a new high-fidelity methodology for predicting entry flows with coupled radiation and ablation is described. The prediction methodology consists of an axisymmetric, nonequilibrium, Navier-Stokes flow solver loosely coupled to a radiation prediction code and a material thermal response code. The methodology is used to simulate the 12.6-km/s Earth atmospheric entry of the Stardust sample return capsule using ablating and nonablating boundary conditions. These flow simulations are used to size and design the Stardust forebody and afterbody heatshields and develop arcjet test conditions and models. The flow simulations indicate that the afterbody heating and pressure profiles in time are significantly different than the forebody heating and pressure profiles. This result is explained in terms of the pertinent aerothermodynamics of the flowfield and the vehicle's geometry. When applied to the afterbody thermal protection system, these results show that the traditional afterbody heatshield design approach is nonconservative for the Stardust sample return capsule shape and entry conditions.

Nomenclature

A	= area, m
B'	= nondimensional mass blowing coefficient
C_d	= drag coefficient
D	= sample return capsule (SRC) diameter, m
$\bar{D}$	= reference diffusion coefficient, m^2/s
$\mathcal{D}_{ij}$	= multicomponent diffusion coefficient
F_i	= diffusion factor for species i
k	= Boltzmann constant, J/K
L	= SRC length, m
M	= Mach number
$\mathcal{M}$	= molecular weight, g/g-mole
$\dot{m}$	= surface mass flux, kg/m^2-s
p	= surface pressure, N/m^2
Q	= integrated heatload, J/m^2
q	= total surface heat flux, W/cm^2
q_{conv}	= surface convective heat flux, W/cm^2
q_{diff}	= surface diffusive heat flux, W/cm^2
q_{rad}	= surface radiative heat flux, W/cm^2
$\mathcal{R}$	= universal gas constant, J/(mol K)
R_{c1}	= shoulder corner radius, m
R_{c2}	= afterbody corner radius, m
R_n	= nose radius, m
s	= surface distance, m
T	= translational temperature, K
T_v	= vibrational temperature, K
t	= time, s
u, v	= velocity components in x and y, m/s
x, y	= direction components, m
Θ_v	= characteristic vibrational temperature, K
θ_a	= afterbody cone angle, deg
θ_f	= forebody cone angle, deg
μ_s	= species viscosity, kg/m-s
ρ	= mixture density, kg/m^3
$\bar{\Omega}^{(1,1)}_{(N_2,N_2)}$	= average N_2–N_2 collision cross section, m

Presented as Papers 97-2474 and 97-2477 at the AIAA 32nd Thermophysics Conference, Atlanta, GA, June 23–25, 1997, and as Paper 98-0167 at the AIAA 36th Aerospace Sciences Meeting, Reno, NV, Jan. 12–15, 1998; received Feb. 1, 1998; revision received Aug. 15, 1998; accepted for publication Feb. 22, 1999. Copyright © 1999 by the American Institute of Aeronautics and Astronautics, Inc. No copyright is asserted in the United States under Title 17, U.S. Code. The U.S. Government has a royalty-free license to exercise all rights under the copyright claimed herein for Governmental purposes. All other rights are reserved by the copyright owner.

*Research Scientist, Reacting Flow Environments Branch, MS 230-2. Senior Member AIAA.

†Research Scientist, Thermal Protection and Materials Branch, MS 230-2. Member AIAA.

‡Senior Consultant, Thermosciences Institute. Associate Fellow AIAA.

Introduction

EXTRATERRESTRIAL sample return, the ability to return physical samples to Earth for detailed analysis, is a growing part of planetary and solar system exploration. The use of sample return technology stems from the scientific and mission tradeoffs between in situ and terrestrial sample analysis. The mass of the required instrumentation to perform in situ analysis and to relay the information back to Earth and the scientific merits of this analysis are weighed against the mass of the equipment needed to return the sample to Earth and the scientific merits of terrestrial sample analysis.

One method for returning an extraterrestrial sample is a direct entry at Earth using a sample return capsule (SRC). Currently, there are six missions in various stages of development that include Earth sample returns. These missions are Stardust,[1] Muses-C,[2] Aladdin, Genesis, Champollion, and Mars Sample Return[3]; they are intended to return samples from the tail of a comet, an asteroid, the moons of Mars, the solar wind, the surface of a comet, and the surface of Mars, respectively.

General characteristics of this direct entry sample return approach are as follows. First, the SRC must survive a high-speed Earth entry with large aerothermal and structural loads; the minimum entry velocity is 11 km/s. Depending on the mission, the velocities can approach 15–16 km/s. Second, the mass of the SRC must be minimized to minimize the launch costs and to maximize the sample mass return. Because the SRC is transported from Earth to a site where samples are deposited in the SRC and then back to Earth, the sample mass and the launch costs are closely coupled to the mass of the SRC; as the mass of the SRC increases, the launch mass related to the SRC increases exponentially.

The impetus for this paper is the design of the SRC for the Stardust Discovery-class mission. Stardust is scheduled for launch in early 1999 and to return to Earth in early 2006. The prime scientific objective of the mission is to rendezvous with comet Wild-2, gather samples of cometary particles from its tail, and return them to Earth for further analysis. Another objective of the mission is to collect interstellar dust. The purpose of collecting the cometary particles and interstellar dust is to better understand the composition and evolution of the solar system. It is the first attempt at a sample return beyond the Earth–moon system.

The captured cometary particles are stored in the Stardust SRC. The SRC enters Earth's atmosphere with an inertial velocity of approximately 12.6 km/s, the fastest Earth entry of a manufactured object ever attempted, and decelerates to 0.6 km/s in 2 min. At a low supersonic Mach number, a parachute is deployed for a land-based recovery in Utah. The focus of this paper is on the numerical simulation of the flowfield environment and the thermal protection system (TPS) material response during entry. These calculations are applied to the design of the forebody and afterbody heatshields. The paper describes the details of this new high-fidelity simulation

methodology, the role of the calculations in the SRC design process, and the aerothermodynamics of the flow calculations.

Role of Aerothermodynamics in the Stardust SRC Design Process

For the Stardust mission, the high-fidelity entry flow simulations were an integral part of the design process. Predictions of surface shear, pressure, heat transfer, and integrated heat load were used to size the forebody and afterbody heatshield, to estimate design margins, and to develop appropriate arcjet test conditions and test models. The arcjet models were tested at conditions that simulated the predicted entry extremes for flight qualification of five heatshield components: 1) the phenolic-impregnated ceramic ablator (PICA) forebody heatshield,[4] 2) the silicone elastomeric charring ablator (SLA-561V) afterbody heatshield,[5] 3) the afterbody vent, 4) the parachute seal, and 5) the PICA/SLA-561V interface seal. Further, predictions of the flow composition including ablation products were used in contamination studies for the vent design, as well as an environmental impact statement. Finally, the surface recession predictions were used in the aerodynamic[6] and stability[7] analyses for the SRC.

The major design constraints and issues that relate to the aerothermodynamic predictions are as follows. First, the forebody and afterbody heatshields must survive the extreme entry heating environment; during Earth entry, the flow in the forebody is radiating, the heatshield material is ablating, and the ablation products and hot gases from the forebody are recompressed in the wake of the vehicle. Second, the temperature of the carbon composite structure must be kept low enough (below the cure temperature) to prevent structural strength degradation. Third, the temperature of the canister containing the captured cometary and interstellar particles must not exceed 343 K during any portion of the Earth entry. Fourth, two vents are located on the afterbody for pressure relief on ascent and entry. These vents must survive entry, prevent flow contaminates from entering the SRC, and remain unclogged to trigger the barometric switch for parachute deployment. Finally, seals located between the forebody and the afterbody heatshield and on the backplate for the parachute must survive the Earth entry.

For the Stardust SRC heatshield design, entry flow simulations, material response and arcjet testing were closely coupled. For example, arcjet testing was used to determine the overall material response of PICA and to develop an appropriate ablation model. The PICA ablation model was used in the entry flow simulations. The entry flow simulations were used to generate an integrated heatload, which was used to size the forebody heatshield. Moreover, the simulations were used to determine arcjet test conditions to certify the PICA heatshield would withstand the Stardust SRC entry conditions. The nature of the fluid–TPS coupling is material dependent. Thus, the forebody and afterbody TPS materials are discussed briefly in the following paragraphs.

The forebody heatshield material, PICA, is a lightweight ceramic ablator, which was recently developed at NASA Ames Research Center by Tran et al.[8] The Stardust SRC is the first flight application of this material. PICA, however, is a candidate TPS material for the Genesis and Mars sample return missions. In previous planetary missions with high entry heatloads and pressures, such as Pioneer Venus or Galileo, carbon–phenolic has been used as the ablative heatshield material. For Stardust, PICA is being used for three reasons: 1) it is less dense than carbon–phenolic (0.22–0.32 g/cm^3 compared to 0.96–1.6 g/cm^3 for carbon–phenolic), 2) it has a much lower thermal conductivity than carbon–phenolic, and 3) it has a similar ablation performance. Because of these properties, the heatshield and insulation mass requirements for a PICA heatshield are significantly reduced compared to a carbon–phenolic heatshield. Carbon–phenolic, however, was developed to withstand very high pressures, on the order of 10 atm. For Stardust, the peak entry pressure is near 0.5 atm. Therefore, the high mechanical strength capabilities afforded by carbon–phenolic heatshield are not needed. For Stardust, PICA is an enabling technology because the mission cost and weight constraints could not have been met using a heavier carbon–phenolic heatshield.

SLA-561V, which was used on the forebody of the Viking vehicles and the Mars Pathfinder lander, is employed for the Stardust afterbody heatshield. PICA is used on the forebody because it is most effective as an ablator at high heat transfer rates. On the afterbody, the heat transfer rates are much lower; the peak afterbody heat transfer rate is almost two orders of magnitude less than the peak stagnation heat transfer rate. For this environment, SLA-561V is a more suitable ablator.

Procedure

Simulation Strategy

To numerically simulate the Stardust SRC entry flowfield, a number of physical phenomena must be considered. First, to obtain a good estimate of the heat transfer and integrated heat load on the forebody, PICA ablation is modeled; the forebody ablation products are also modeled in the wake. Second, the flowfield transport and chemistry models are formulated to include ablation products. Finally, the effects of radiative heating including radiation from the ablation products are simulated. In the present study, the two-temperature, nonequilibrium, axisymmetric flow solver GIANTS,[9] the nonequilibrium optimized vectorizable radiation process model (NOVAR),[9] and the thermal response code FIAT[10] are modified to simulate the described entry physics.

Using GIANTS/NOVAR/FIAT, the entry trajectory is discretized at 11 points, and laminar flow solutions with radiation are generated for the full SRC configuration using two boundary conditions: 1) no ablation with a fully catalytic wall at the radiative equilibrium temperature for the forebody and afterbody and 2) PICA ablation on the forebody with PICA ablation products in the wake flow and a fully catalytic wall at the radiative equilibrium temperature on the afterbody; based on available transition criteria, it was concluded the flow would remain laminar during the entry heat pulse. The nonablating calculations were used for determining arcjet test conditions whereas the ablating calculations were used for the TPS sizing calculations. Forebody TPS sizing predictions are presented in this work. During entry, the afterbody TPS is ablating. Nevertheless, ablation from the afterbody TPS are not considered. To the authors' knowledge, the work presented in this study is the most extensive database of full-body Navier–Stokes flow simulations ever generated for a high-speed, ablating, entry probe, and it is the first time Navier–Stokes calculations of this type have been used to define the afterbody aerothermal environment through the entire heat pulse.

An effort is made to describe and explain interesting aerothermodynamic features of the forebody and afterbody flow environments. Also, a number of aerothermodynamic phenomena such as ablation and geometry effects are investigated in depth via parametric variation of important modeling quantities. These calculations are described in the present work and in Refs. 11–13.

For the forebody flow calculations, the radiation, flow simulation, and ablation methodologies used in this study are derived from two main sources: computational comparisons with Fire II flight data and the TPS sizing calculation for the Mars Pathfinder mission. Fire II was a flight experiment carried out for the Apollo program in 1965 (Ref. 14). The capsule entered the Earth's atmosphere at 11.35 km/s using a series of three nonablating beryllium heatshields; measurements of the total stagnation heating, including radiation intensity, were made. For Fire II and Stardust, the peak nonablating heat transfer rate, vehicle diameter, and length of the heat pulse are similar. In Ref. 9, comparisons with the Fire II data were used to assess the accuracy of the methodologies used in this study for predicting radiation and convective heat transfer on the forebody; numerical predictions of the stagnation heat transfer and radiation intensity using GIANTS/NOVAR were in good agreement with the Fire II flight data.

The ablation coupling strategy used in this work was developed by Chen et al.[15] for the TPS sizing of the Mars Pathfinder aeroshell. In Ref. 15, GIANTS and the charring material ablator (CMA)[16] code (FIAT is derived from CMA) were combined in a loosely coupled manner to size the Mars Pathfinder SLA-561V forebody heatshield; arcjet data were used to develop and validate the SLA-561V ablation model used in the calculations.

In Ref. 17, coupled Navier–Stokes calculations with ablation and radiation were used to analyze the possible accidental entry of the

Cassini spacecraft during its Earth gravity-assist maneuver. Also, coupled radiation and ablation solutions have been generated using viscous shock layer[18] and boundary-layer[19,20] methods. Yet, to the authors knowledge, the work presented in this study is the first time that Navier–Stokes flow calculations with coupled radiation and ablation have been used as the primary tool for a heatshield design.

For the afterbody calculations, the computational resources needed for a Navier–Stokes simulation of a wake flow are much greater than for a forebody flow simulation; a laminar Navier–Stokes wake flow simulation usually requires at least an order of magnitude more computational resources than the forebody. This resource requirement has limited the number of wake flow simulations performed in the past. Also, because the heating in the wake is typically 1–2 orders of magnitude lower than the forebody, it is less critical to accurately compute the wake region.

For the Mars Pathfinder afterbody heatshield design, Mitcheltree and Gnoffo[21] generated wake flow solutions at two trajectory conditions including one at angle of attack using the SLA-561V ablation products from the forebody; the afterbody heatshield was assumed to be nonablating. In Ref. 22, full-body solutions around the Mars Pathfinder aeroshell at four trajectory points were generated; ablation effects, however, were neglected.

For computational fluid dynamics (CFD) validation purposes, the amount of flight data with afterbody heating measurements is limited; base pressure was measured during entry on the Viking landers,[23] afterbody TPS thermocouple measurements were made for Mars Pathfinder,[24] and some afterbody heating and pressure data exist from the Apollo program.[25] In a recent experiment by Hollis and Perkins,[26] forebody and afterbody heating measurements were made on a sting-mounted 70-deg sphere–cone in air and CO_2; the measured forebody stagnation heating rates were about 1200 W/cm^2 in air and 800 W/cm^2 in CO_2, which are similar to the Stardust nonablating and ablating peak heating rates. Comparisons of the measured wake heating with Navier–Stokes computations[27] were usually within the experimental error range except for small regions of the recirculation zone. The computational methodology used in Ref. 27 is very similar to the methods used in this work. Thus, it is believed that this comparison provides some validation for the wake calculations in this study. In Ref. 28, Gnoffo generated laminar wake flow solutions for the aeroassisted flight experiment and compared them with experimental data; predictions of the wake heating were in good agreement with the experimental data.

Fluid Flow Governing Equations

A set of governing equations is developed that is appropriate for the high-velocity Earth entry heating environment of the Stardust SRC. The appropriate fluid dynamic equations for a entry flow have been described in a number of sources.[29–32] As a baseline, the calculations without ablation employ an 11-species air model consisting of N_2, O_2, NO, N, O, N_2^+, O_2^+, NO^+, N^+, O^+, and e^-. The effects of thermal and chemical nonequilibrium are simulated. To model thermal nonequilibrium, separate vibrational and total energy equations are included; the electronic energy modes are not simulated. Thus, the total Navier–Stokes equation set is represented by 11-species densities equations, two total momentum equations, a total energy equation, and a vibrational energy equation. Solutions to this equation set for axisymmetric flows are obtained using the Gauss–Seidel procedure of Candler[32] and Candler and MacCormack.[33]

To account for PICA ablation, an 18-species model, consisting of CO_2, CO, N_2, O_2, NO, C_2, C_3, CN, H_2, HCN, C, N, O, H, C^+, N^+, O^+, and e^-, is used. The transport, vibrational relaxation and chemical models used for the 18-species equation set are described in the following paragraphs. The chemistry and transport models used for the 11-species set are given in Refs. 9 and 34 and will not be discussed except to note differences in the modeling between the 18- and 11-species sets.

Transport

The mixture viscosity and thermal conductivity are calculated using Wilke's[35] semi-empirical mixing rule with curve fits for the species viscosities extended from Blottner et al.[36] The Ref. 36 curve fits were used for N_2, O_2, NO, N, and O. Curve fits for the species viscosities for CO_2 and CO using the Lennard–Jones 6–12 potential were generated by Candler in Ref. 37. Following a similar procedure, Lennard–Jones' curve fits are generated for C_2, C_3, CN, HCN, H_2, H, and C. The species viscosities for the ions C^+, N^+ and O^+ are assumed equal to their corresponding neutral. The coefficients for the viscosity curve fits are given in Table 1.

Table 1 Species viscosities curve fits for 18-species model

	$\mu_s = 0.1\exp[(A_s \ell_n T + B_s)\ell_n T + C_s]$			
Species	A_s	B_s	C_s	Reference
CO_2	−0.019527387	1.047818	−14.32212	37
CO	−0.019527394	1.013295	−13.97873	37
N_2	0.0268142	0.3177838	−11.3155513	36
O_2	0.0449290	−0.0826158	−9.2019475	36
NO	0.0436378	−0.0335511	−9.5767430	36
C_2	−8.4311e−3	0.7876060	−13.0268000	11
C_3	−8.4312e−3	0.7876090	−12.8240000	11
CN	−8.3811e−3	0.7860330	−12.9406000	11
H_2	−8.3346e−3	0.7815380	−13.5351000	11
HCN	−2.4241e−2	1.0946550	−14.5835500	11
C	−8.3285e−3	0.7703240	−12.7378000	11
N	0.0115572	0.6031679	−12.4327495	36
O	0.0203144	0.4294404	−11.6031403	36
H	−8.3912e−3	0.7743270	−13.6653000	11
C^+	−8.3285e−3	0.7703240	−12.7378000	11
N^+	0.0115572	0.6031679	−12.4327495	36
O^+	0.0203144	0.4294404	−11.6031403	36

Species diffusion is modeled using a bifurcation approximation,[38–40] which has been shown to compare well with exact solutions of Stefan–Boltzmann equations[40] and work well for both Earth and Mars atmospheres.[39] In the model, binary diffusion coefficients are approximated as

$$\mathcal{D}_{i,j} = \bar{D}/F_i F_j \tag{1}$$

where $\bar{D}$, F_i, and F_j can be functions of both temperature and pressure. Applying the bifurcation approximation, expressions for the species mass fluxes are obtained that are similar to Fick's law in both form and computational cost; the bifurcation model, however, is a closer representation of the Stefan–Boltzmann equations. Details of the implementation are found in Refs. 34 and 38–40.

The curve fits for F_i and F_j are obtained assuming a reference diffusion coefficient $\bar{D}$ and then performing a least-squares curve fit over all of the binary diffusion coefficients for a given temperature and pressure. This procedure is repeated at various temperatures and pressures to generate a curve fit of $F_i(T, p)$. In Refs. 38 and 39, it is shown that the temperature and pressure variations of the F_i are not large, and it is a reasonable approximation to assume that the F_i are constant; the temperature and pressure variations are accounted for in $\bar{D}$. In the present study, the self-diffusion of N_2, $\mathcal{D}_{N_2,N_2}$, is used for $\bar{D}$ as[41]

$$\bar{\Omega}^{(1,1)}_{(N_2,N_2)} = \frac{8}{3}\sqrt{\frac{\mathcal{M}_{N_2}}{\pi \mathcal{R} T}}\, 10^{-20} T^{-0.274} 190.3757, \qquad \rho\bar{D} = \frac{kT}{p\bar{\Omega}^{(1,1)}_{(N_2,N_2)}} \tag{2}$$

The F_i for the 11-species model were curve fitted in Ref. 34 using the least-squares procedure. In the present study, F_i values in the 18-species model are obtained from three sources: Where the 18- and 11-species models overlap, values of F_i are taken from Ref. 34; for the remainder of the species, F_i are estimated from Refs. 38 and 39 noting that $\bar{D}_{O_2,O_2}$ is used as the reference diffusion coefficient in these sources. This procedure is used because a comprehensive set of cross section data of a similar level of fidelity is not available for the 18-species model. The authors believe that using a least-square curve fit procedure for the 18-species model with cross section data of widely varying accuracy would not increase the fidelity of the simulation. The F_i values used are given in Table 2. By the use of Eqs. (1) and (2) and Table 2 with the bifurcation approximations,[38] the diffusion transport modeling used in this work is obtained.

The major difference in the transport modeling between the 11- and 18-species models is in the calculation of the viscosity and

thermal conductivities. For the 11-species model, collisional cross section data are used following the formulation of Gupta et al.[41] to calculate the viscosity and thermal conductivity, whereas the 18-species model uses viscosity curve fits with Wilke's mixing rule and a Eucken relation to calculate these quantities. To determine the effects of the modeling on the heat transfer predictions, nonablating calculations are made using both models and are presented in the "Results" section. In this paper, both nonablating and ablating calculations are performed using the 18-species transport and chemistry model except for the cases where geometry effects are studied.

Chemistry, Vibration, Radiation Models

The 18-species reaction model developed consists of 9 dissociation reactions, 8 exchange reactions, and 3 electron impact ionization reactions. The prime source for the forward reactions and equilibrium constants is Park.[30,42] The reaction set used in this study is summarized in Table 3; sources[30,42–46] and the temperatures used in the reactions are noted. The use of Park's two-temperature model is indicated by $\sqrt{(TT_v)}$. Further, dissociation efficiencies for a number of species are assumed and, following Park,[42] the electron impact ionization rate for C is assumed equal to that of O. A significant difference between the 18-species model and the 11-species model is that the ions N_2^+, O_2^+, and NO^+ and their charge exchange reactions are dropped from the 18-species model; based on their small mass fraction in the flow, these ions were removed from the chemistry model to reduce the computational cost of the full-body calculations. A comparison of the heat transfer using the 11- and 18-species models is shown in the "Results" section.

Table 2 F_i and species diffusion factors for the 18-species model

Species	F_i
CO_2	1.35
CO	1.06
N_2	1.0
O_2	1.06279
NO	1.03073
C_2	0.95
C_3	1.12
CN	1.06
H_2	0.3
HCN	1.2
C	0.6
N	0.580012
O	0.63559
H	0.2
C^+	0.75
N^+	0.747927
O^+	1.02257
e^-	1.0

For all polyatomic species except for CO_2, vibrational–translational relaxation times are calculated using the relaxation rates of Millikan–White[47]; for CO_2, the rates of Camac[48] are used. The vibrational energy modes are calculated using a harmonic oscillator model. Characteristic vibrational temperatures and degeneracy levels are obtained from a number of sources[32,37,49,50]; these values are given in Table 4.

The radiation module used in this study is NOVAR; NOVAR was developed from the LORAN code[51] and validated against the Fire II flight data using an 11-species air model.[9] NOVAR calculates line, continuum, and molecular radiation using a tangent slab transport model. To account for ablation products, C line and molecular CO, C_2, CN, and CO_2 bands are added to the various air and molecular bands; emission and absorption by these species is modeled. The effects of H line radiation are neglected.

Surface Boundary Conditions

The fluid–TPS interface is modeled using mass and energy balances. A number of different assumptions are made regarding the surface boundary conditions. For the 11-species, nonablating calculations, the forebody and afterbody surfaces are assumed to be fully catalytic to N, O, and ion recombination at the radiative equilibrium wall temperature. An emissivity of 1.0 is employed for all of the calculations using the radiative equilibrium wall assumption.

Table 3 Chemistry model

Reaction	M	$K_f = CT_x^n \exp(-T_d/T_x)$, cm^3 mol^{-1} s^{-1}				Reference source
		T_x, K	C	T_d, K	n	
Dissociation reactions						
$CO_2 + M \rightarrow CO + O + M$	M_{vib}[a]	$\sqrt{(TT_v)}$	6.9^{21}	63,275	−1.5	42
$CO_2 + M \rightarrow CO + O + M$	$M_{atom,\,ion}$[b]	$\sqrt{(TT_v)}$	1.4^{22}	63,275	−1.5	42
$CO + M \rightarrow C + O + M$	M_{vib}[a]	$\sqrt{(TT_v)}$	2.3^{20}	129,000	−1.0	42
$CO + M \rightarrow C + O + M$	$M_{atom,\,ion}$[b]	$\sqrt{(TT_v)}$	3.4^{20}	129,000	−1.0	42
$N_2 + M \rightarrow N + N + M$	M_{vib}[a]	$\sqrt{(TT_v)}$	7.0^{21}	113,200	−1.6	42
$N_2 + M \rightarrow N + N + M$	$M_{atom,\,ion}$[b]	$\sqrt{(TT_v)}$	3.0^{22}	113,200	−1.6	42
$N_2 + M \rightarrow N + N + M$	e^-	$\sqrt{(TT_v)}$	1.0^{25}	113,200	−1.6	42
$O_2 + M \rightarrow O + O + M$	M_{vib}[a]	$\sqrt{(TT_v)}$	2.0^{21}	59,750	−1.5	42
$O_2 + M \rightarrow O + O + M$	$M_{atom,\,ion}$[b]	$\sqrt{(TT_v)}$	1.0^{22}	59,750	−1.5	42
$NO + M \rightarrow N + O + M$	M_{vib}[a]	$\sqrt{(TT_v)}$	5.0^{15}	75,500	0.0	42
$NO + M \rightarrow N + O + M$	$M_{atom,\,ion}$[b]	$\sqrt{(TT_v)}$	1.1^{17}	75,500	0.0	42
$C_2 + M \rightarrow C + C + M$	M_{vib},[a] $M_{atom,\,ion}$[b]	$\sqrt{(TT_v)}$	3.7^{14}	69,000	0.0	42
$C_3 + M \rightarrow C_2 + C + M$	M_{vib},[a] $M_{atom,\,ion}$[b]	$\sqrt{(TT_v)}$	6.3^{16}	101,200	−0.5	43
$CN + M \rightarrow C + N + M$	M_{vib},[a] $M_{atom,\,ion}$[b]	$\sqrt{(TT_v)}$	2.5^{14}	71,000	0.0	42
$H_2 + M \rightarrow H + H + M$	M_{vib},[a] $M_{atom,\,ion}$[b]	$\sqrt{(TT_v)}$	2.2^{14}	48,300	0.0	44
Exchange reactions						
$NO + O \rightarrow N + O_2$	——	T	8.4^{12}	19,450	0.0	42
$N_2 + O \rightarrow NO + N$	——	T	6.4^{17}	38,370	−1.0	42
$CO + O \rightarrow O_2 + C$	——	T	3.9^{13}	69,200	−0.18	42
$CO_2 + O \rightarrow O_2 + CO$	——	T	2.1^{13}	27,800	0.0	42
$CO + C \rightarrow C_2 + O$	——	T	2.0^{17}	58,000	−1.0	42
$CO + N \rightarrow CN + O$	——	T	1.0^{14}	38,600	0.0	42
$N_2 + C \rightarrow CN + N$	——	T	1.1^{14}	23,200	−0.11	42
$CN + O \rightarrow NO + C$	——	T	1.6^{13}	14,600	0.10	42
$CN + C \rightarrow C_2 + N$	——	T	5.0^{13}	13,000	0.0	42
$HCN + H \rightarrow CN + H_2$	——	T	8.0^{11}	85,537	0.0167	45
Electron impact ionization reactions						
$C + e^- \rightarrow C^+ + 2e^-$	——	T	6.35^{15}	130,700	0.0	46
$N + e^- \rightarrow N^+ + 2e^-$	——	T	5.08^{16}	121,000	0.0	46
$O + e^- \rightarrow O^+ + 2e^-$	——	T	6.35^{15}	106,200	0.0	46

[a] CO_2, CO, N_2, O_2, NO, C_2, C_3, CN, H_2, and HCN. [b] C, N, O, H, C^+, N^+, and O^+.

Table 4 Harmonic oscillator vibrational constants

Species	Θ_v, K	g
CO_2	1903	1.0
—	945.0	2.0
—	3329.0	1.0
CO	3074.0	1.0
N_2	3395.0	1.0
O_2	2239.0	1.0
NO	2817.0	1.0
C_2	2668.6	1.0
C_3	1845.0	1.0
—	778.7	2.0
—	3117.6	1.0
CN	2976.26	1.0
H_2	6332.5	1.0
HCN	4762.5	1.0
—	1024.2	2.0
—	3016.2	1.0

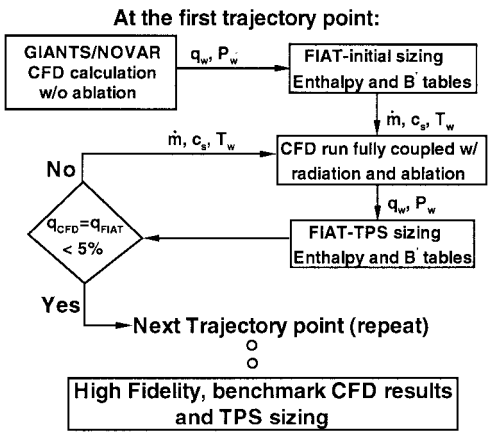

Fig. 1 Ablation and radiation coupling strategy.

For the 18-species, ablating calculations, the forebody is assumed to be ablating, whereas the afterbody is nonablating. For the ablating forebody, the procedure to be described for matching the boundary condition between the flow and material thermal response solvers produces a CFD boundary condition that is easy to implement. At the fluid–surface interface, the pressure at the first cell above the surface from the previous iteration is used as the surface pressure. With prescribed values of the surface pressure, mass fractions, and temperature known (the surface mass fractions, temperature, and blowing rate are fixed inputs from FIAT) a surface density is calculated. With the surface density and blowing rate, a normal wall velocity is generated. The surface velocity, mass fractions, and density determine the mass injection rate and surface diffusion rate.

Two nonablating boundary conditions are used for the afterbody. First, the afterbody is assumed to be fully catalytic to N, O, and, ion recombination at the radiative equilibrium wall temperature. Second, the afterbody is assumed to be fully catalytic to CO, N, and ions at the radiative equilibrium wall temperature. The CO catalysis is modeled using the methodology of Mitcheltree and Gnoffo.[52] CO catalysis effects are included because a large CO mass fraction develops in the wake region as a result of forebody ablation. The effects of forebody ablation including parametric variation of the blowing rate are described in the "Results" section. As noted earlier, the ablation products from the afterbody TPS are not modeled.

Radiation and Ablation Coupling

The ablation and radiation modules are loosely coupled with the flow solver. The coupling procedure for a trajectory-based TPS sizing with ablation and radiation is shown in Fig. 1. At the first trajectory point in time, a CFD solution with coupled radiation is generated; values of the wall heat transfer rate and pressure are passed to FIAT. The initial CFD solution at each trajectory point is generated assuming a fully catalytic radiative equilibrium wall boundary condition. Next, the material response, enthalpy, and B' tables are generated from the initial CFD input; FIAT models the in-depth conduction, blowing, pyrolysis, and surface recession of the PICA heatshield material as a function of time. (The PICA ablation model was developed from arcjet test data.) Next, assuming the mixture of gas constituents at the surface of the ablator from the fluid and the ablator are in equilibrium at the temperatures and pressures predicted from FIAT, a blowing rate, mass fractions for the 18-species model, and wall temperature are calculated and passed to GIANTS/NOVAR; the equilibrium surface composition is calculated using the MAT code.[53] A new CFD solution with radiation and ablation is calculated, and new values of the wall heat transfer rate and pressure are passed to FIAT. A new heat transfer rate is calculated and compared with the old CFD value. If the difference between the CFD and FIAT heat transfer rates is greater than 5% at any of the surface locations, then the new values of the mass fraction, wall temperature, and blowing rate are passed to the CFD solver, and the procedure is repeated.

In the present calculations, a maximum of three global iterations was required at each trajectory point to meet the prescribed heat transfer convergence criterion. The 5% tolerance is fairly conservative because it is triggered if the difference between the CFD and FIAT heat transfer rates at any surface location is greater than 5%. With three global iterations, most of the surface points were well below the 5% criterion. A lower tolerance would require more iterations. With the heat transfer criterion satisfied, the boundary condition at the fluid–surface interface between GIANTS/NOVAR and FIAT is matched, and the coupled flowfield and material response problem is modeled.

Once convergence is obtained, the procedure described in the preceding paragraphs is repeated at the next trajectory point in time starting with a CFD/NOVAR solution without ablation. As the global solution advances in time, the material response from the previous trajectory points are used by the FIAT code. Thus, the temporal history of the material response is included in the global GIANTS/NOVAR/FIAT calculation. The accuracy of the method in time is a function of the number of points used along the trajectory. Between trajectory points, a linear interpolation is used for the temperature and heat transfer by FIAT. The authors believe that the seven points used to discretize the trajectory in this study are adequate.[15] A time discretization refinement study, however, has not been performed. (In Ref. 54, the coupled CFD/material thermal response of a nonablating wing leading edge using GIANTS and a boundary element code is presented. A refinement study of the time discretization showed that the coupled CFD/material response problem was not very sensitive to the number of trajectory anchor points.)

After the global iteration scheme over the entire trajectory is completed, the integrated heatload is calculated and a heatshield thickness distribution is generated. FIAT also provides estimates of the surface recession rate. The shape change of the forebody is not incorporated in the CFD calculations. Using additional iterations between FIAT and GIANTS/NOVAR, however, it would be possible to incorporate the effects of the surface recession. (Estimates of the surface recession are used in the calculations of the Stardust SRC aerodynamics by Mitcheltree et al.[6])

The algorithm for coupling radiation to the flowfield is described in Refs. 9 and 34. For the flow calculations in this study, the radiative energy in the flow is relatively small; the maximum radiative component is about 10% of the total stagnation heating during the entry heat pulse. Flow calculations at peak heating demonstrated that the coupling between the radiation and the flowfield is minimal. Thus, the flowfield radiation coupling term is not considered. Nevertheless, the radiative heating at the surface affects the ablation characteristics of the material, which alters the flowfield.

Results

The primary heatshield design trajectory for the Stardust SRC[1] uses an 8-deg entry flight-path angle and a 70-kg/m^2 ballistic coefficient with conservative estimates of the atmospheric structure and the SRC's drag; This overshoot trajectory produces the maximum

Table 5 Freestream flow conditions

Time, s	Altitude, km	Relative velocity, m/s	Density, kg/m^3	Temperature, K	Chemistry no. of species
34	81.64	12590.4	$9.63e^{-6}$	216.93	18
42	71.92	12413.4	$4.16e^{-5}$	221.42	18, 11
48	65.44	12004.0	$1.06e^{-4}$	229.0	18, 11
54	59.77	11136.7	$2.34e^{-4}$	238.47	18, 11
58	56.50	10245.7	$3.62e^{-4}$	245.37	11
60	55.02	9718.71	$4.39e^{-4}$	248.48	18, 11
64	52.37	8560.23	$6.18e^{-4}$	252.71	11
66	51.19	7956.9	$7.21e^{-4}$	253.55	18, 11
70	49.10	6769.5	$9.48e^{-4}$	255.05	11
76	46.51	5178.9	$1.35e^{-3}$	256.90	18, 11
80	45.05	4298.7	$1.65e^{-3}$	255.99	11

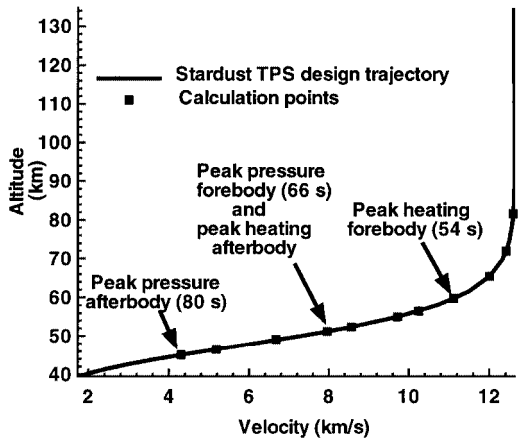

Fig. 2 Stardust heatshield design trajectory.

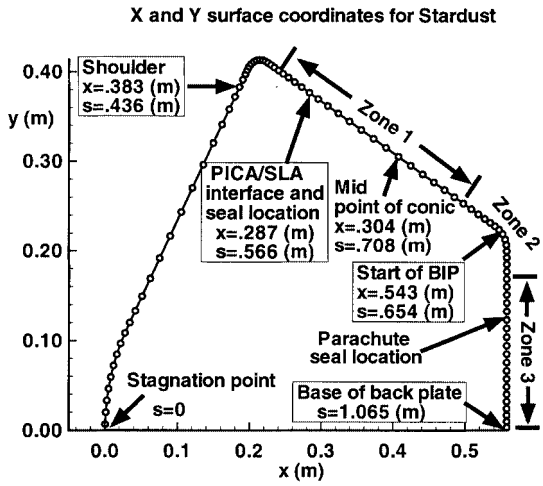

Fig. 3 Surface geometry and surface locations of interest for the Stardust SRC.

heatloads. (The effects of mass loss due to ablation or shape change were not coupled to the trajectory propagation.) The heat pulse is short, on the order of 1 min, but the peak stagnation heat transfer rate is large; thus, the total integrated heatload is also large. This entry trajectory is plotted in Fig. 2 with the simulated trajectory points denoted by squares; the velocity scale is Earth relative. For this trajectory, peak heating and pressure on the afterbody occur at approximately 54 and 66 s, respectively. The peak heating and pressure on the afterbody occur at a different time in the trajectory. This result is discussed in detail. The freestream conditions at the simulated trajectory points are listed in Table 5.

The surface geometry for the Stardust SRC heatshield design calculations is plotted in Fig. 3. The forebody is an axisymmetric 60-deg sphere–cone with a nose radius of approximately 23 cm. The afterbody geometry is a 30-deg cone. The interface between the forebody and afterbody heatshields is denoted by the PICA/SLA-561V interface. To collect the comet dust, the forebody heatshield opens like a clamshell. Thus, a seal must be designed at this point to prevent hot-gas incursion into the interior of the vehicle. Another seal exists for the opening of the parachute; the parachute also must be protected from hot-gas incursion during entry. The parachute canister is anchored to the back interference plate (BIP), shown in Fig. 3.

Grids for the full-body calculations (forebody and afterbody) were 145 × 81. The SRC was discretized by 89 points and the wake centerline by 56 points (145) and 81 points normal to the surface. For the forebody and afterbody flows, grid resolution and adaptation effects are presented in Refs. 11 and 12 for the 54- and 60-s trajectory conditions. It was concluded from these calculations that the 145 × 81 grid resolution was adequate.

The results in this section are presented in two parts: forebody and afterbody. For the forebody, a few major topics of discussion are the flow modeling, aerothermodynamics, surface quantities used for the heatshield design, and TPS sizing. For the afterbody, a few major topics of discussion are the surface quantities used for the heatshield design, aerothermodynamics, geometry effects, and the influence of the forebody ablation products on the afterbody flow environment.

Forebody Aerothermodynamics and TPS Sizing

In this section, predictions of the forebody aerothermal environment along the Stardust TPS design trajectory and the forebody TPS sizing calculations are presented. The first three issues discussed are the effects of ablation on the flowfield, the convergence of the ablative heat transfer, and the effects of the different chemistry and transport modeling assumptions between the 18-species ablating and 11-species nonablating equation sets; peak heating conditions are used for all of these calculations. Next, for calculations with and without ablation, surface heat transfer, pressure, and shear along the forebody's surface and in time are examined, and the importance of these quantities to the heatshield design are described. Finally, the integrated heatload and PICA thickness and total surface recession distributions used for the SRC forebody heatshield design are presented.

Flow Modeling and Ablation Effects

The effects of ablation and chemistry modeling on the flowfield and surface heat transfer are described, and the convergence of the simulation methodology is examined (Figs. 4–8). For all of the calculations except for those in Fig. 7, the nonablating and ablating calculations employ the 18-species equation set that is described in the "Procedure" section. The boundary condition for the nonablating solutions, which are used to determine the arcjet test conditions, is a fully catalytic wall at the radiative equilibrium temperature; the arcjet test conditions are calibrated using a nonablative copper calorimeter.

Figure 4 is a plot of the pressure, temperature, and velocity along the stagnation line at peak heating for calculations with and without ablation. As expected, surface ablation moves the shock away from the surface, but properties in the inviscid region such as the peak temperature and pressure are unaffected by ablation. In Fig. 5, the surface mass injection rate at the stagnation point, its components, and the ratio of mass injection rate to the freestream mass flux are

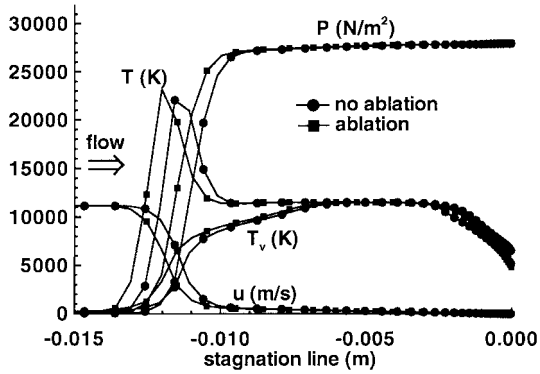

Fig. 4 Comparison of stagnation properties for calculations with and without ablation at peak heating.

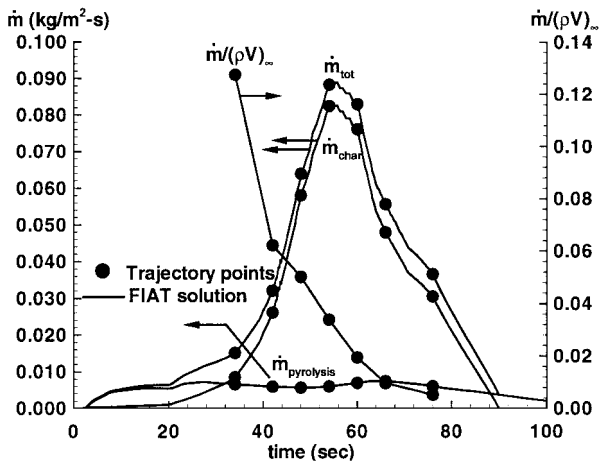

Fig. 5 Predicted stagnation blowing rate and blowing rate components vs time.

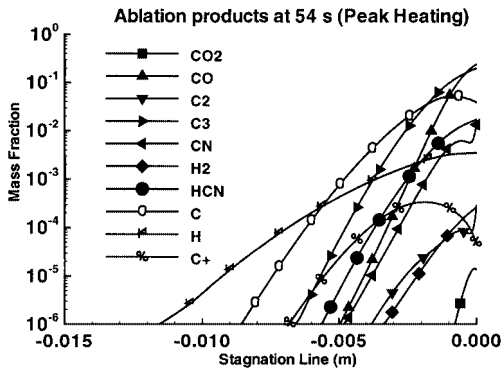

Fig. 6 Ablation products along the stagnation line at peak heating.

plotted. At peak heating, where the peak mass injection rate occurs, the surface blowing rate is only about 3% of the freestream mass flux. The maximum ratio occurs early in trajectory; it is about 13% at 34 s and decreases as the SRC descends into the atmosphere. Thus, the effects of the mass injection on the shock standoff distance are more pronounced earlier in the trajectory. The blowing gases from PICA consist primarily of char with a small amount of pyrolysis gas.

In Fig. 6, the mass fractions of the ablation products along the stagnation line are plotted. The dominant ablation species by mass are C_3 and CO; secondary ablation products are C, HCN, CN, and H. Via surface blowing and diffusion, the ablation species diffuse about halfway across the shock layer. This penetration is larger earlier in the trajectory, when the blowing rates are a larger fraction of the freestream mass flow.

In Fig. 7, the total convective surface heat transfer and its components along the forebody are plotted for the 18-species and 11-species equation sets. Both calculations employ a nonablating, fully catalytic, radiative equilibrium wall boundary condition. The differences in the models produce cancelling effects with q_{conv}

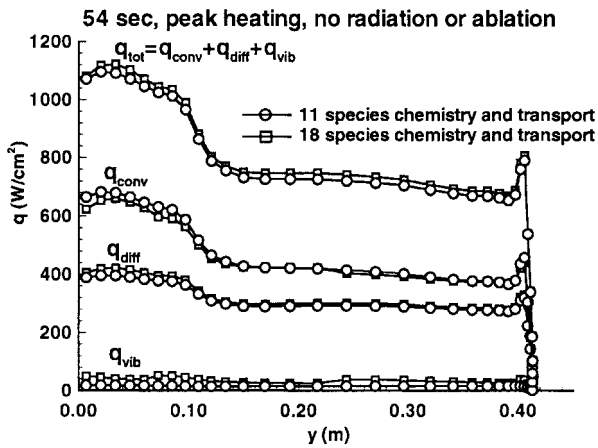

Fig. 7 Comparison of nonablating heat transfer components at peak heating for the 18- and 11-species formulations.

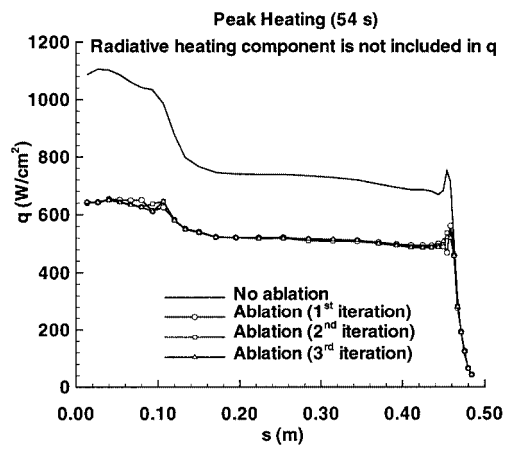

Fig. 8 Convergence of heat transfer at peak heating.

higher but q_{diff} lower for the 11-species model. Overall, the heat transfer for the 18-species model is slightly higher. At the stagnation point, the maximum difference is about 2%. In Fig. 7, there is slight dropoff in the heat transfer as the stagnation line is approached. The dropoff is the result of numerical difficulties at the axis of symmetry; grid adaptation removes this error.[11,12]

Finally, in Fig. 8, the convergence of the ablative convective heat transfer is plotted; the radiative heat transfer component is not included in Fig. 8. The ablative solution is started from the nonablative, fully catalytic, flow calculation. After one iteration, the heat transfer at most of the points is within the 5% convergence criterion. The largest oscillations occur at the sphere–cone junction and the shoulder, where large changes in the flow gradients along the surface occur. The second and third global iterations are needed to converge the ablation solutions at these points. The total computational cost for the nonablating solution and three global iterations is about 1 CPU hour on the Cray C-90.

Surface Heating, Pressure, and Shear

Surface quantities used in the design of the Stardust heatshield are examined. Figure 9 shows the total nonablating forebody heat transfer in time at the seven trajectory points. The peak heat transfer rate is about 1200 W/cm^2. This heating value with a 25% margin[55] was used as one of the arcjet test conditions for qualifying the PICA heatshield.[4] In Fig. 10, the radiative component of the total heat transfer is plotted. The radiative component is about 10% of the total heating at the stagnation point and 7% at the shoulder. The rise in the radiative heat transfer at the shoulder at the 48- and 54-s conditions is a result of a large number of N and O atoms in the shock layer at these conditions.

In Fig. 11, the total forebody ablative heat transfer at each time in the trajectory is plotted. These profiles follow the shape of the nonablating heat transfer in Fig. 9, but the magnitude of the heating,

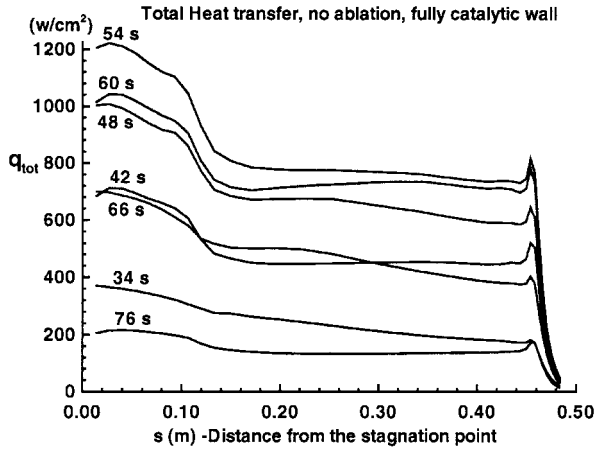

Fig. 9 Total nonablating forebody surface heat transfer rates over time, 18 species.

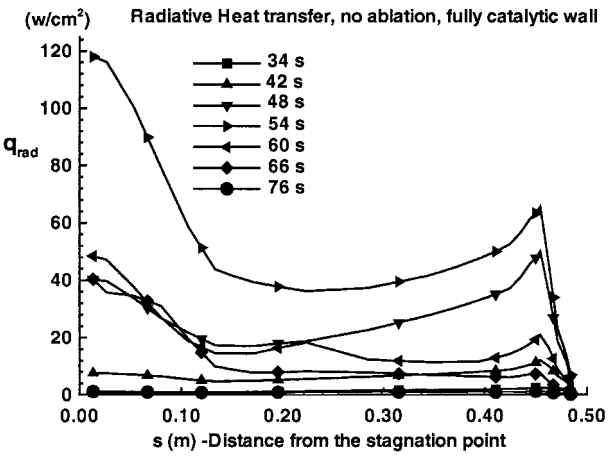

Fig. 10 Radiative component of the total nonablating forebody heat transfer rate over time.

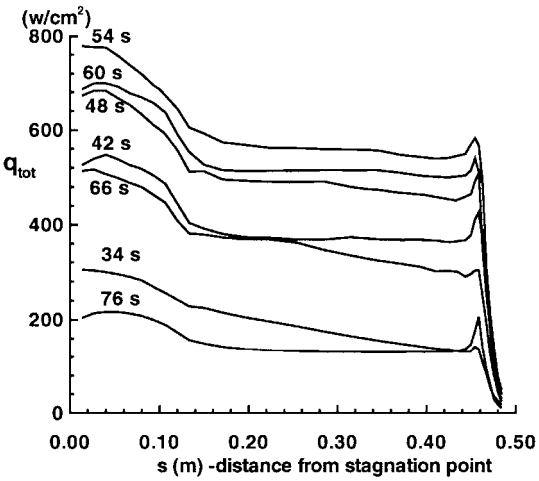

Fig. 11 Total ablating forebody surface heat transfer rates over time, 18 species.

as expected, is reduced by ablation. These heat transfer distributions are used in FIAT to size the PICA heatshield. The reduction in heat transfer from ablation is clearly shown in Fig. 12, which is a plot of the total ablating and nonablating heat transfer rates near the stagnation point. At peak heating, the reduction in heating is about 35% of the nonablating total. After peak heating, where the blowing rate is lower (see Fig. 5), blockage by ablation vapors is less effective.

Figure 13 shows the heat transfer components near stagnation point used in Fig. 12. The reduction in heat transfer from ablation is a result of a decrease in the diffusive heating. With ablation, the surface mass fractions of N and O, which are fully recombined at

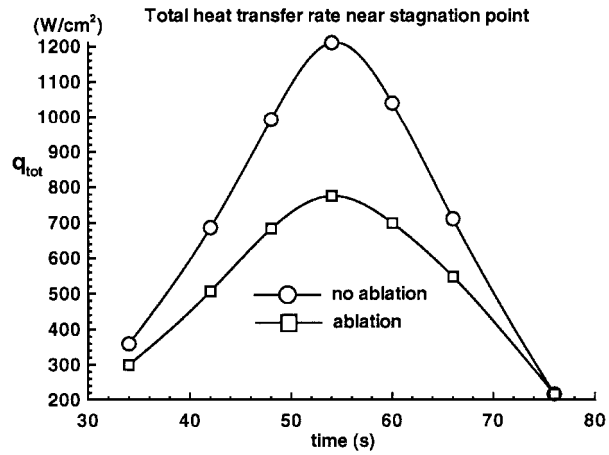

Fig. 12 Comparison of the total nonablating and ablating heat transfer rates vs time near the stagnation point.

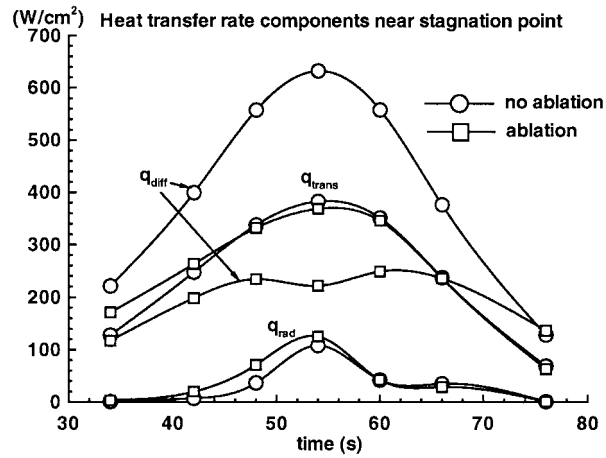

Fig. 13 Comparison of the nonablating and ablating heat transfer components vs time near the stagnation point.

the wall for the nonablating calculation, are much lower. Further, the mass injection of CO, which is a major ablation product (see Fig. 6), significantly lowers the wall enthalpy. The dip in the diffusive heating curve near peak heating results because PICA becomes a more effective ablator with increasing heat transfer rate.[8] The radiative component of the heating decreases much faster in time than the convective component. With ablation, the radiative heat transfer rate is slightly increased before peak heating despite accounting for absorption of radiation by ablation vapors. A significant fraction of the increase in radiation is from the C line and $CO(4^+)$ molecular radiation. At the 42- and 48-s conditions, the relative blowing rate as a ratio of the freestream mass flux is higher than later in the trajectory; thus, CO and C penetrate deeper into the shock layer, and the radiation from C and CO is increased.

In Fig. 14, wall temperature near the stagnation point is plotted. The nonablative radiative equilibrium wall temperature is reduced from 3735 to 3380 K at peak heating. The temperature is reduced through the formation of the ablation gas, in-depth conduction, and the reduction in enthalpy carried to the surface. For the nonablating case, where the wall is assumed to be insulated, in-depth conduction would also lower the surface temperature. Typically, in-depth conduction reduces the surface temperature by about 50–100 K depending on the material and the shape of the heat pulse.

The heat transfer, pressure, and surface shear are the three primary quantities used for establishing the arcjet test conditions needed for flight qualification. The performance ranges for each of these quantities is a function of the TPS material, and the entry trajectory is tailored to satisfy these material requirements. For example, the formulation of PICA employed on the Stardust SRC is useful for pressures up to 0.6 atm. Near 0.6 atm and above, the material begins to spall as a result of localized mechanical failures. When spallation

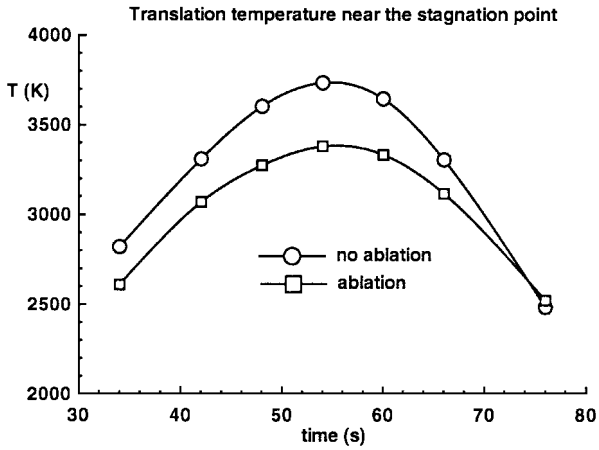

Fig. 14 Comparison of the nonablating and ablating surface temperatures vs time near the stagnation point.

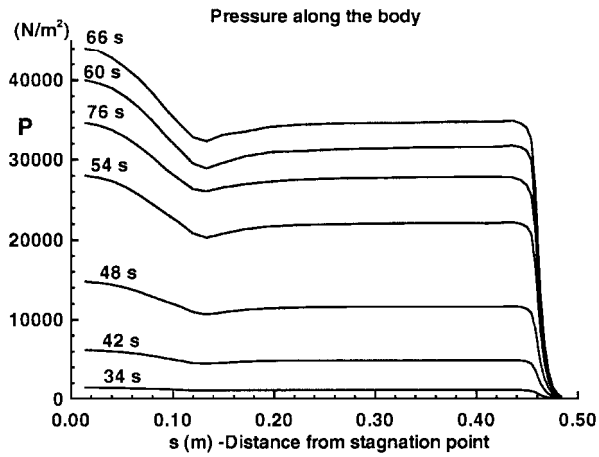

Fig. 15 Surface forebody pressures in time for the nonablating calculation.

occurs, the ablation properties of the material are generally nonuniform and difficult to predict; spallation occurs when pieces of the heatshield are ejected as a result of thermomechanical stresses. With a weight penalty, the mechanical strength and maximum pressure limit of PICA can be increased by increasing the global density of the material or using surface densification.

In Fig. 15, the forebody pressure in time is plotted. A peak pressure of about 44,000 N/m^2 occurs at the 66-s conditions. This pressure is below the PICA limit. In Fig. 16, the pressure vs time near the stagnation point is shown for both ablating and nonablating calculations. The introduction of ablation products does not significantly affect the surface pressure.

Figure 17 is a plot of the surface shear along the forebody at 60 s; the maximum surface shear occurs at this time for both the ablating and nonablating calculations. Ablation reduces the surface shear by reducing the normal velocity gradient at the surface. In Fig. 18, the peak shear (located near the shoulder) is plotted vs time. The reduction in the peak shear is about 25%. The surface shear was examined to determine if it exceeded the PICA material limits. If the magnitude of the shear is too large, then spallation may occur. The present calculations predict that the peak shear is within acceptable limits for the PICA material used on the Stardust SRC.

Integrated Heatload, TPS Sizing, and Surface Recession

Finally, with the ablative heat transfer rate predicted as a function of time, the surface distribution of integrated heatload is calculated, and the PICA heatshield is sized. Figure 19 shows a plot of the total, convective, and radiative surface integrated heatload vs time. The heatload at the stagnation point is approximately 28,000 J/cm^2, which is on the order of the heatload at the Shuttle stagnation point. The Shuttle heat pulse, however, is about 20 times longer and much

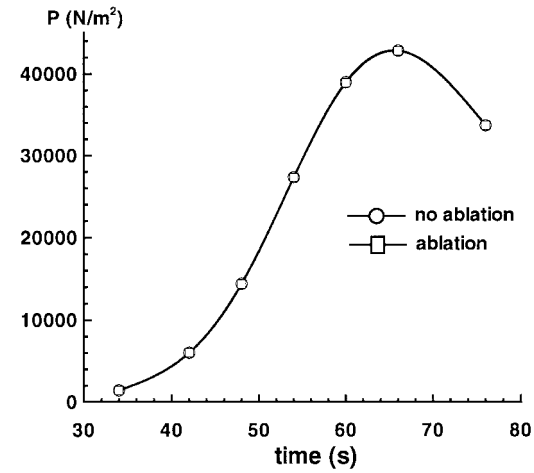

Fig. 16 Comparison of the nonablating and ablating surface pressure vs time near the stagnation point.

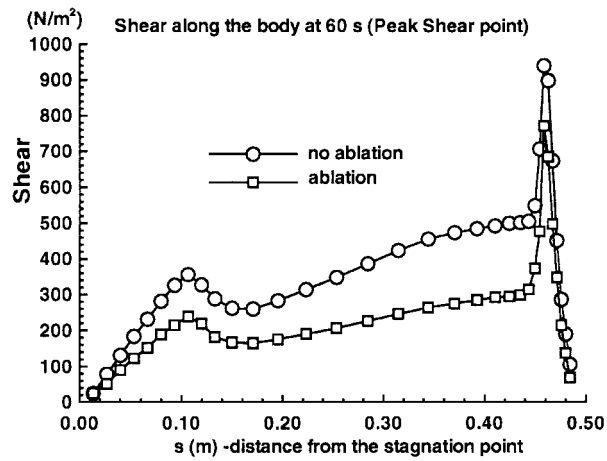

Fig. 17 Comparison of the nonablating and ablating surface shear at 60 s along the forebody.

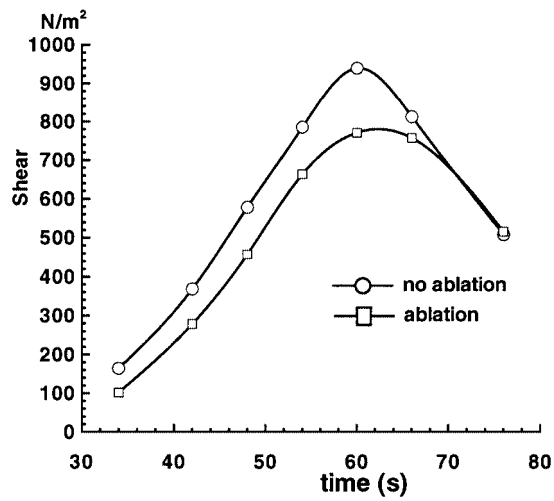

Fig. 18 Comparison of the nonablating and ablating peak surface shear vs time near the shoulder.

flatter. Most of the total heatload is the result of boundary-layer convection; the maximum radiative heatload, which occurs at the stagnation point, is only about 7% of the total. At peak heating, the radiative heat transfer component is about 20% of the total ablative heat transfer rate; however, the profile of the radiative heat transfer rate curve in time is narrower than the convective heating profile (see Figs. 10 and 13). Thus, the radiative fraction of the integrated heatload is reduced.

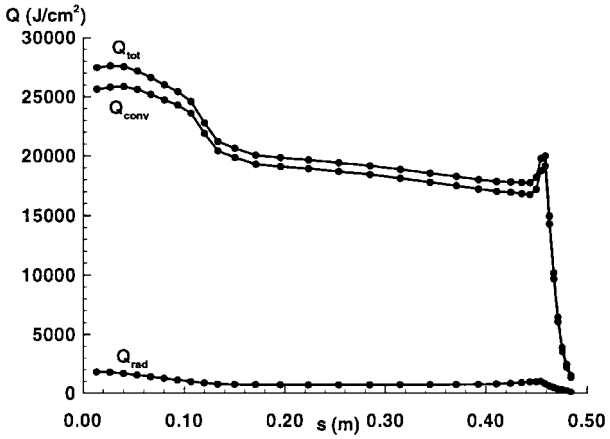

Fig. 19 Predicted integrated heatloads for the Stardust SRC forebody.

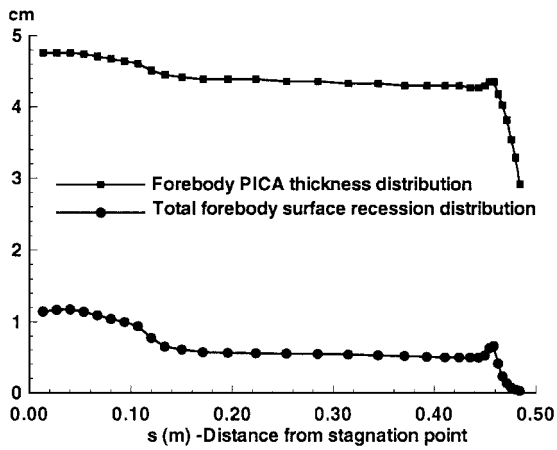

Fig. 20 Forebody PICA thickness and total surface recession distributions.

The integrated heatload is used to size the PICA heatshield thickness using the initial internal temperature of the SRC prior to entry and a specified temperature limit for the carbon composite structure. The surface thickness and total surface recession distributions are plotted in Fig. 20. By comparing the total heatload and surface thickness curves, it is seen that the surface thickness curve is relatively flat; the large local changes in heatload in the nose region and at the shoulder do not produce a corresponding change in the heatshield thickness. The flatness in the TPS thickness distribution occurs because PICA becomes a more efficient ablator as the heat transfer increases.[8] This thickness distribution with the addition of margin was used to machine a block of PICA for the Stardust SRC heatshield.

In Fig. 20, the surface recesses about 1 cm near the nose and 0.5 cm on the cone; the recession at the nose is about 4% of the 23-cm nose radius. The stagnation convective heat transfer rate is approximately inversely proportional to the square root of the nose radius. Thus, the maximum increase in the heat transfer rate from surface recession is about 2% [$\sqrt{(23/22)}$]. Therefore, it is concluded that the effect of the surface recession on the predicted PICA thickness distribution is insignificant. For the aerodynamics,[6] however, the small reduction in the vehicle's diameter from surface recession at the shoulder does reduce the total drag force.

Afterbody Aerothermodynamics

Full-body CFD (forebody and wake) calculations are presented with and without ablation. One calculation requires between 20 and 35 CPU hours on a Cray C-90 depending on the chemistry model; this compares with 1 h for a calculation with ablation on the forebody. For the calculations with ablation, an 18-species chemistry and transport model is used. Without ablation, an 11-species chemistry and transport model is used. Again, the trajectory locations where these models are employed to generate flow solutions are listed in Table 5. To better refine the afterbody heating and pressure profiles in time, additional nonablating flow solutions are computed at 58, 64, 70, and 80 s. Also, to better understand the afterbody aerothermodynamics, additional nonablating flow calculations are generated for a number of perturbations of the Stardust geometry.

The wake results are presented in four sections. First, general wake flow characteristics and afterbody surface pressure and heat transfer distributions with and without forebody ablation are described. Second, the relationship between the afterbody surface pressure and heat transfer distributions and the aerothermal environment is discussed. Third, vibrational nonequilibrium and geometry effects on the wake aerothermal environment are studied. Finally, the effects of the forebody ablation products including CO catalysis on the wake aerothermal environment are examined.

Wake Flow Characteristics and Surface Pressure and Heat Transfer Distributions

Figure 21 is a plot of the laminar wake streamlines for the Stardust SRC at peak heating. Four wake flow features are 1) a large single recirculation region bounded by a shear layer, 2) the forebody bow shock, which extends into the wake, 3) an inviscid expansion region between the bow shock and shear layer, and 4) a flow separation near the end of the conic section of the afterbody. This structure is typical for a laminar wake.[56]

In Figs. 22–27, variations of surface pressure and heating distributions in time for the calculations with and without ablation are presented at the base of the backplate, start of the BIP, and the PICA/SLA interface (see Fig. 2). In Fig. 3, three zones are indicated.

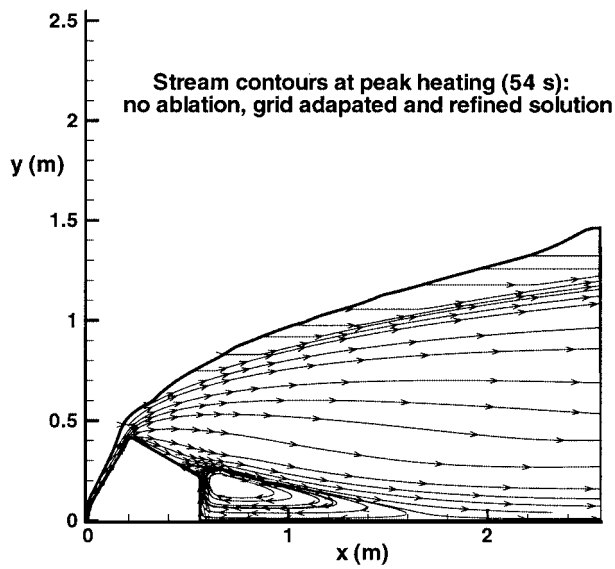

Fig. 21 Laminar wake streamlines for the Stardust SRC.

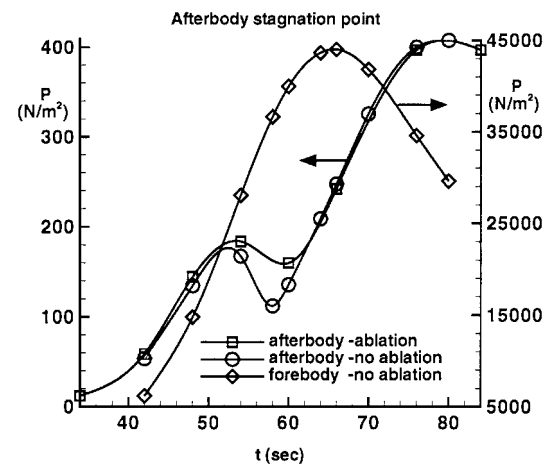

Fig. 22 Afterbody base pressure profiles with and without forebody ablation products and the forebody stagnation-point pressure profile.

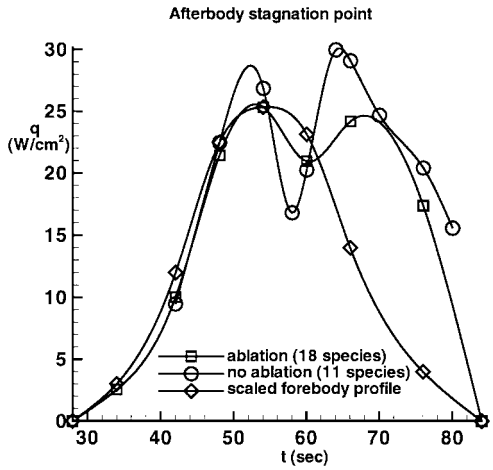

Fig. 23 Afterbody base heat transfer profiles with and without forebody ablation products and a scaled heat transfer profile based on the forebody stagnation heat transfer.

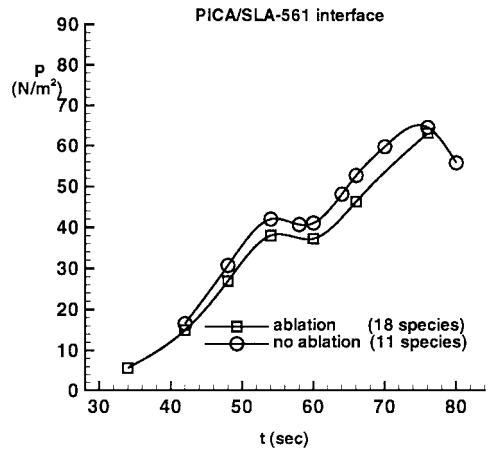

Fig. 24 Pressure profiles at the PICA/SLA-561V interface with and without forebody ablation products.

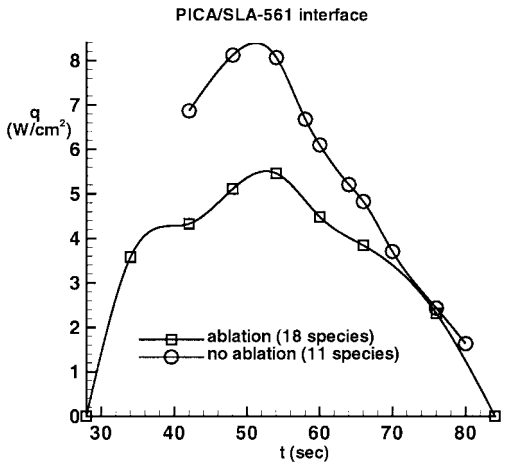

Fig. 25 Heat transfer profiles at the PICA/SLA-561V interface with and without forebody ablation products.

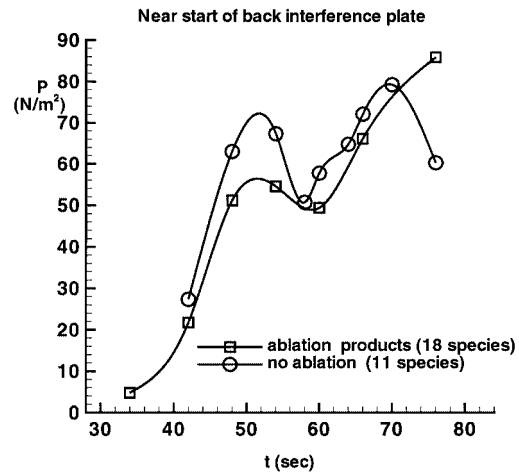

Fig. 26 Pressure profiles at the BIP interface with and without forebody ablation products.

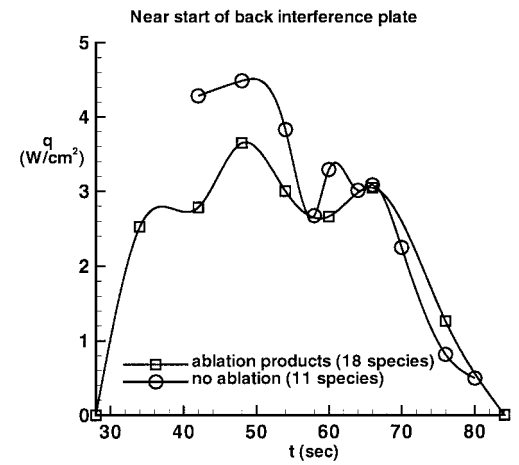

Fig. 27 Heat transfer profiles at the BIP interface with and without forebody ablation products.

The PICA/SLA interface is in zone 1 (Figs. 24 and 25), the start of the BIP is in zone 2 (Figs. 26 and 27), and the base of the backplate is in zone 3 (Figs. 22 and 23). The surface pressure and heating profiles shown at each location are characteristic of the other profiles that lie within the same zone, although the magnitude of the surface quantities vary at each location and the profiles blend smoothly into one another along the surface. Finally, in Figs. 22–27, the surface pressure and heating profiles are curve fit using a cubic spline; the solid lines are the spline fit, and the open symbols are the predicted values from the computations. For the ablating heating profiles, the surface heat transfer is assumed to be zero at 28 and 84 s for the cubic spline fits; flow calculations are not generated at these points. Finally, the calculations with ablation assume an afterbody surface that is fully catalytic to N, O, and atoms. In the wake, as a result of forebody ablation, the CO mass fraction is significant. The effects of CO catalysis are described later in this section.

Figure 22 is a plot of pressure profiles vs time near the base of the backplate with and without the forebody ablation products and a plot of the stagnation pressure profile that is with and without ablation; the scale for each curve is indicated by the arrow. A number of important observations are made from Fig. 22. First, the peak in pressure for the afterbody occurs about 14 s later in the trajectory than on the forebody. Second, the rise in the afterbody pressure is not monotonic; a dip and a second higher peak occur in the pressure profile. Third, the forebody ablation products lead to a rise in pressure as a result of mass addition. Finally, early and late in the trajectory, when the amount of mass addition is small (see Fig. 5), the nonablating and ablating pressures are similar. The first two observations are unexpected and have not been previously reported or explained in the literature. An explanation of this behavior is deferred to the following sections.

Stardust afterbody heating profiles vs time near the base of the backplate are plotted in Fig. 23. Three curves are presented: 1) with the forebody ablation products, 2) without the forebody ablation products, and 3) an afterbody heating curve calculated by scaling from the forebody heating distribution. The scaled heating profile is representative of a traditional afterbody heatshield design methodology; the forebody and afterbody heating profiles are assumed to have the same shape with the peak afterbody heating some fraction of the forebody peak heating. The calculations indicate that this is not a good assumption. For the ablating and nonablating calculations,

the heat pulse is longer in the afterbody, and like the pressure, a dip occurs in the profile. For the nonablating calculations, which are more refined in time, the peak heating value on the afterbody occurs later in the trajectory than it does on the forebody.

In Fig. 23, the nonablating and ablating heating profiles are different. The peaks of the ablating profile are lower, and the dip between the peaks is not as extreme as for the nonablating profile. Ablation and catalysis effects are discussed in more detail later.

The results presented in Figs. 22 and 23 have a number of implications for the afterbody heatshield design. The afterbody heat pulse is longer, which increases the integrated heat load. In Fig. 23, the nonablating heat transfer curve is used to size the Stardust SRC afterbody heatshield. The extended heat pulse increases the heat load by approximately 30% as compared to the scaled profile. This additional heat load increases the heatshield mass. Further, the heating design margins for the afterbody are quite large.[55] To account for computational uncertainties relating to turbulence and angle-of-attack effects, the heating profiles on the base of the afterbody are scaled by a factor of 3.5; the scaled heating values are used for developing arcjet test conditions and performing the TPS sizing calculations. Thus, the design peak heating value for the base of the Stardust SRC afterbody is 90 W/cm^2. This peak heating value compares with 25 W/cm^2 for the stagnation point of the Viking forebody or 40–50 W/cm^2 for the stagnation point of the Shuttle. Fortunately, the length of the Stardust heat pulse is much shorter than for either Viking or the Shuttle.

Another implication of the results in Figs. 22 and 23 is that the traditional afterbody heatshield design approach[21,22] is nonconservative for the Stardust SRC capsule shape and trajectory. The traditional afterbody heatshield design approach assumes that the forebody and the afterbody heating and pressure profiles are similar, i.e., the peak afterbody pressure and heating values occur at the same forebody trajectory times and the shape of the profiles are the same. Therefore, wake calculations are generated at the forebody peak heating and pressure trajectory locations. Afterbody pressure and heating profiles are generated by scaling the forebody profiles using the predicted peak afterbody values. As already described, the forebody and afterbody heating and pressure profiles are different. Further, the present results indicate that the peak wake pressure and heating values occur later in the trajectory for the afterbody. Thus, for the Stardust SRC, the traditional approach underpredicts peak wake heating and pressure values, as well as integrated heat load. It is shown later that the afterbody heating is a function of the forebody and afterbody geometry and that scaling the afterbody heating profiles from the forebody heating profiles is a crude approximation.

In Figs. 24–27, the characteristic heating and pressure profiles for zones 1 and 2 are described. Figure 24 is a plot of the pressure at the PICA/SLA-561 interface. Similar to the predictions for the base of the afterbody, a dip in the pressure is observed, and the peak pressure occurs after the forebody peak. The nonablating pressure, however, is higher; this result is discussed in the following sections. Heat transfer profiles are shown in Fig. 25. At the PICA/SLA-561V interface, the double peaks in the heat transfer curve that occur at the base of the afterbody do not occur; the shape is closer to a forebody profile (see Fig. 23) with the peak heating value on the afterbody occurring at the same trajectory location as the forebody. Again, the heat transfer with ablation is lower.

Figure 26 is a plot of the pressure at the start of the BIP. The pressure profiles display the double hump profile. The nonablative pressure profile is higher than the ablative profile. The heat transfer profiles are shown in Fig. 27. These curves display numerous oscillations. At the BIP interface, a complex flow interaction occurs involving a flow expansion, shear layer, flow recirculation, and flow separation. It is likely that this location is very sensitive to grid density. Thus, grid effects may be producing the oscillations, or the separation region may be moving as the trajectory conditions change.

Relationship Between the SRC Aerothermal Environment and the Afterbody Heating and Pressure Profiles

An explanation of the afterbody heating and pressure distributions is a difficult task. Flow particles reaching the base of the afterbody travel through the bow shock, expand around the shoulder, travel along the conic afterbody, expand into the wake, and then are recompressed and stagnated at the base of the afterbody. The flow is in chemical nonequilibrium, thermal nonequilibrium, and radiating. Further, complex chemical interactions involving ablation products and the ionized, dissociated, and vibrationally excited shock flow are occurring. These effects are highly coupled. Thus, isolating individual contributions is difficult.

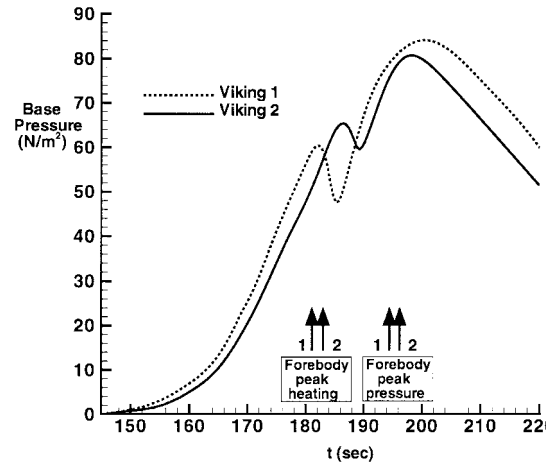

Fig. 28 Base pressure profiles for the Viking landers.

Before posing an explanation, flight data from the Viking 1 and 2 landers and Mars Pathfinder are presented as partial validation of the afterbody results described in the preceding section. Figure 28 is a plot of base pressure on the afterbody measured for the Viking 1 and Viking 2 landers[23]; the forebody geometry for the Viking landers was a 70-deg sphere–cone. The locations of the peak forebody heating and pressure are indicated in Fig. 28. The pressure profiles are very similar to the distributions generated in the present work; a dip in pressure occurs for both flights shortly after peak heating, and the peak in pressure on the afterbody occurs after the forebody peak in pressure. In Ref. 16, the results were left unexplained, attributed to ablation products from the forebody. The Stardust SRC calculations demonstrate that this effect occurs with or without ablation forebody ablation products. For Viking, a similar rise in the heating also was observed. The rise in heating was attributed to turbulent heating, but these calculations show it occurs for laminar flows as well.

Thermocouple measurements from the recent Mars Pathfinder mission also support the results in this work.[24] In Ref. 24, it is shown by Milos et al. that an afterbody heat transfer profile scaled from a forebody profile does not reproduce the thermocouple data on the afterbody. The predicted thermocouple data from the scaled afterbody heat transfer profile are out of phase with the flight data. An afterbody heat pulse, which is longer than the forebody heat pulse, however, produces a predicted thermocouple measurement that matches the flight data. This result is consistent with the afterbody heating profile predicted in this paper for the Stardust SRC.

One thesis, which will be expounded in this section, is that the afterbody heating and pressure profiles are strongly influenced by the shock–expansion interaction at the forebody shoulder. It is believed that the amount of mass ingested into the afterbody conic boundary layer is related to the shock standoff distance at the shoulder. As the bow shock near the shoulder moves away from the body, more mass is ingested into the afterbody conic boundary layer, which is recompressed in the wake recirculation region producing the higher pressures and heating. As the shoulder shock moves toward the body, less mass is ingested in the afterbody conic boundary layer, which lowers the pressure and the heat transfer. In the next two sections, evidence is presented to validate and test this hypothesis.

To explain the afterbody aerothermal environment, flow solutions at different points along the trajectory are compared. The objective of these comparisons is to understand the drop and subsequent rise in heat transfer and pressure in the afterbody base region after the forebody peak heating trajectory conditions. For these comparisons, flow properties are examined along lines normal to the surface at the shoulder and at the midpoint of the conic afterbody (see Fig. 3).

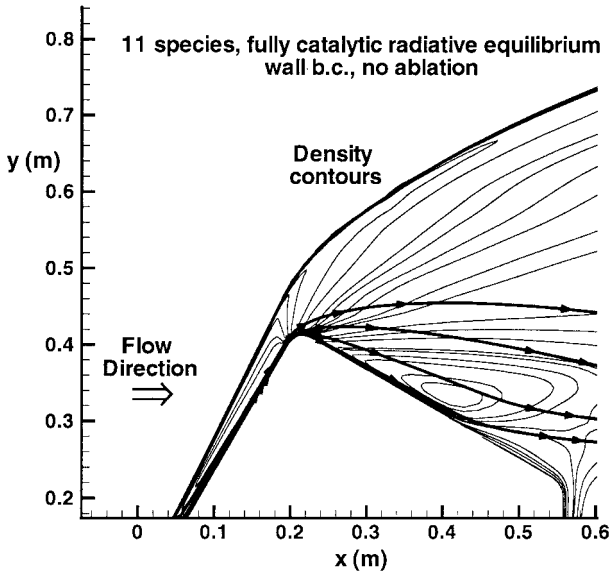

Fig. 29 Density contours and streamlines near the shoulder at peak heating.

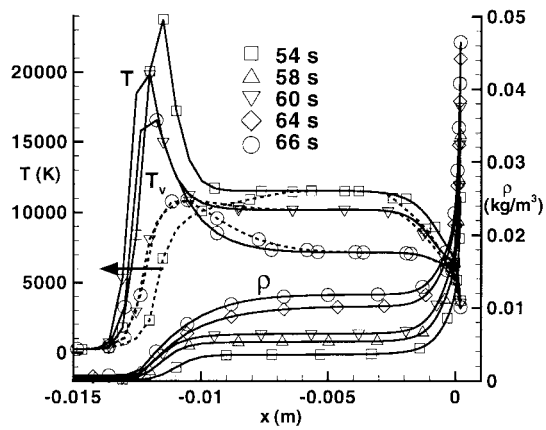

Fig. 30 Comparisons of temperature and density profiles along the stagnation line at various times in the trajectory.

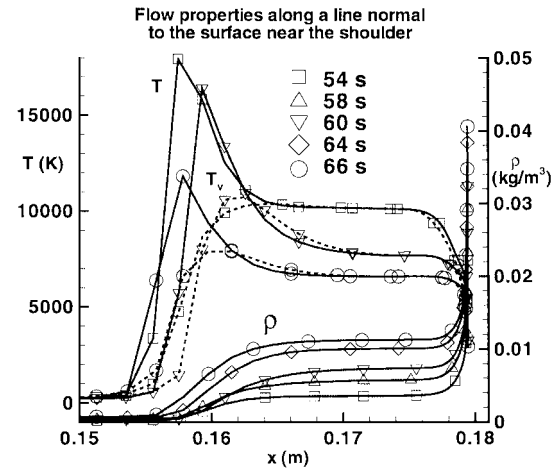

Fig. 31 Comparisons of temperature and density profiles near the shoulder at various times in the trajectory.

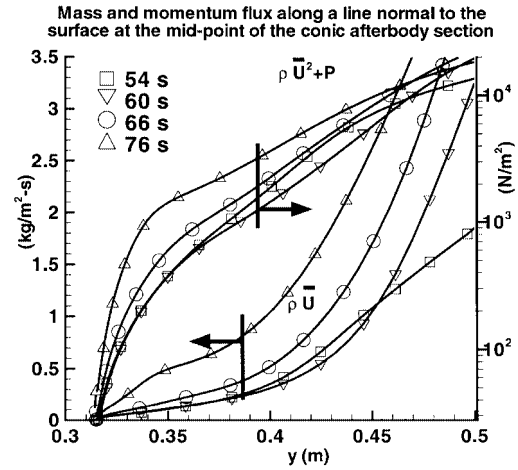

Fig. 32 Mass and momentum fluxes along a line normal to the surface at the midpoint of the afterbody conic section.

Figure 29 shows density contours and streamlines near the shoulder at peak heating. The density contours clearly show the bow shock and shoulder expansion. In the afterbody, the shear layer and recirculation region are separated by a dividing streamline. The mass ingested into the afterbody recirculation region is the sum of the mass that passes between the surface and this streamline. In Fig. 29, it is seen that this streamline must originate in the forebody boundary layer passing very close to the shoulder. The uppermost streamline in Fig. 29, which is clearly in the inviscid expansion region in the wake, passes very close to the shoulder. The dividing streamline must lie below this streamline. Thus, the initial conditions for the afterbody recirculation region begin at the shoulder.

In Figs. 30 and 31, translational temperature, vibrational temperature, and density distributions are plotted at the stagnation line and a line normal to the surface at the shoulder (see Fig. 3) for the trajectory conditions between 54 and 66 s. All of the calculations presented in this section utilize an 11-species chemistry and transport model and the nonablating wall boundary conditions. The 54- and 66-s trajectory conditions bound the dip and rise in pressure on the afterbody base in Fig. 22.

Along the stagnation line in Fig. 30, the density and shock standoff distance increase monotonically in time between peak heating (54 s) and peak pressure (66 s). The shape of the density profiles, however, changes. Progressing from peak heating to peak pressure, the flat region between the rise in density at the shock and near the surface becomes smaller. Further, the rise in density through the shock occurs over a longer length scale. For the temperatures predictions at the 54-, 60-, and 66-s conditions shown in Fig. 30, the rise in density through the shock occurs in a region of thermal nonequilibrium. The change in the density profile for the 66-s calculation corresponds to an overshoot in the vibrational temperature. The shape of the density profile as it rises through the shock, steep (54, 58, and 60 s) or more gradual (64 and 66 s), correlates with the vibrational temperature profile in the nonequilibrium region and whether an overshoot of the postshock vibrational temperature occurs; the shape of the vibrational temperature profile depends on the vibrational relaxation times, the diatomic species concentrations, and, the vibration–dissociation coupling model.

As shown in Fig. 31, at the shoulder the density and shock standoff distance do not increase monotonically in time. At 60 s, the shock standoff distance is smaller than the 54- and the 66-s predictions. Further, the maximum vibrational temperature overshoot occurs at 60 s; along the stagnation line, the maximum vibrational temperature overshoot occurs at 66 s. A corresponding change in the density profile at 60 s is also observed.

At 60 s, the changing shock strength between the stagnation point and the shoulder and the flow path that the particles take to reach the shoulder produce conditions that are more favorable to increased vibrational excitation as compared to the stagnation region. These conditions produce the observed overshoot in the vibrational temperature and the decrease in shock standoff distance. For the 60-s calculation, the relative minimum in shock standoff distance at the shoulder corresponds to the relative minimum in heat transfer and pressure at 60 s. This result is the first piece of evidence that appears to support the hypothesis regarding the relationship between the shoulder flow expansion and afterbody heating and pressure profiles.

Figure 32 shows the mass and momentum fluxes along a line normal to the surface at the midpoint of the conic afterbody between 54

Table 6 Geometry matrix

Geometry	D, m	L, m	R_n, m	θ_f, deg	R_{c1}, m	θ_a, deg	R_{c2}, m
Baseline, 60-deg sphere–cone	0.827	0.5572	0.2286	60	0.01905	30	0.02667
50-deg sphere–cone	0.827	0.5572	0.2286	50	0.01905	30	0.02667
70-deg sphere–cone	0.827	0.5572	0.2286	70	0.01905	30	0.02667
20-deg afterbody	0.827	0.5572	0.2286	60	0.01905	20	0.02667
40-deg afterbody	0.827	0.5572	0.2286	60	0.01905	40	0.02667
200% R_{c1}	0.827	0.5572	0.2286	60	0.0381	30	0.02667
50% R_{c1}	0.827	0.5572	0.2286	60	0.009525	30	0.02667

and 76 s (see Fig. 3); the arrows indicate appropriate scales. At 60 s, there are less mass and momentum fluxes near the surface than at 54 or 66 s; a crossover in the 54- and 60-s mass flux and momentum flux curves occurs. The lower momentum and mass fluxes near the surface lead to the decreased pressure and heating in the afterbody base region observed for the 60-s calculation as compared to the 54-, 64-, or 66-s calculations. It is believed that the crossover in the 54- and 60-s curves is a related to the smaller shock standoff distance at the shoulder for the 60-s calculation. Although not shown, a crossover between the 58- and 54-s curves also occurs. The heating and pressure predicted for the 58-s conditions (Figs. 22 and 23) is lower than that predicted for the 54-s conditions; thus, this result is consistent with the 60-s calculation. Further, the predicted shock standoff distance for the 58-s calculation is also smaller than at 54 s.

Finally, between 60 and 76 s, the shock standoff at the shoulder increases monotonically, the pressure on the base of the afterbody increases monotonically, and, as seen in Fig. 32, the mass and momentum fluxes near the conic afterbody surface increase monotonically. The mass and momentum fluxes do not decrease at 66 s, which is the peak forebody pressure condition. Hence, the times when peak pressure occurs between the forebody and afterbody are shifted. Between 60 and 76 s, the afterbody heating reaches a peak and then decreases (see Fig. 23). This trend occurs because the kinetic energy of the vehicle is rapidly decreasing and, thus, the surface of the forebody is cooling. Therefore, less energy flux is being transported into the afterbody base region. This effect balances the increase in mass and momentum fluxes entering the afterbody as a result of the increase in shock standoff distance at the shoulder.

In summary, it was shown that the afterbody base pressure distributions calculated for the Stardust SRC are in qualitative agreement with the Viking flight data and the afterbody heating vs time profiles are consistent with flight data from Mars Pathfinder; the shape of the base pressure profiles as well as a shift in time for the peak pressure between the forebody and afterbody occur in the Stardust predictions and the Viking flight data. Further, the length of the afterbody heat pulse (the time between the onset and termination of significant heating) in the base region for the Stardust SRC is longer than on the forebody. This phenomenon is consistent with the Pathfinder flight data. It was hypothesized that the shape of the profiles is related to the flow expansion around the forebody shoulder. It was shown that the increases and decreases of the pressure and heating in the base of the afterbody correlate with the increases and decreases of mass and momentum fluxes near the surface of the afterbody conic, which correlate with increases and decreases in the shock standoff distance near the shoulder.

Effect of Vibrational Nonequilibrium and Forebody Geometry on the Wake Aerothermal Environment

To test the hypothesis discussed in the preceding section, two numerical experiments are constructed to alter the character of the flow expansion around the forebody of the shoulder by changing the forebody shock standoff distance. First, to increase the shock standoff distance at the shoulder, the vibrational relaxation times of various flow species are increased. Two additional flow solutions are calculated at the 60-s trajectory conditions: 1) a calculation using the vibrational relaxation times of N_2 increased by a factor of 1000 and 2) a calculation using the vibrational relaxation times of all of the species increased by a factor of 1000. These solutions are compared with the calculation using the standard vibrational relaxation times. The objective of the experiment is to determine if increasing the shock standoff distance via increased vibrational relaxation times increases the pressure and heating profiles in the afterbody. Second, full-body flow solutions are generated at the 54-s, peak heating conditions, with the SRC geometry altered to change the forebody shock standoff distance near the shoulder. The objective of these cases is to determine the relation between the forebody geometry, which affects the shock standoff distance, and the afterbody pressure and heating profiles. Seven forebody geometry perturbations are considered and are listed in Table 6. All of the calculations in this section employ the 11-species chemistry model with the nonablating radiative equilibrium wall boundary condition.

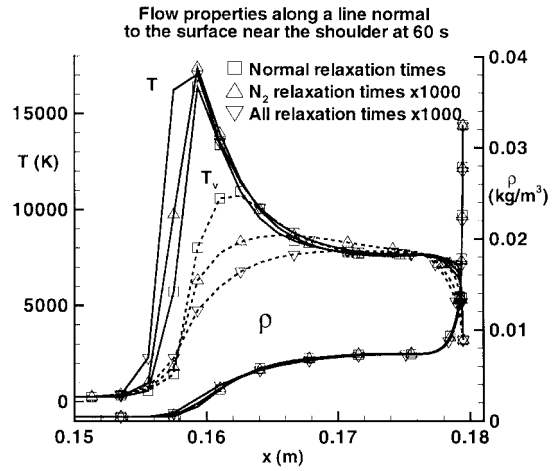

Fig. 33 Comparisons of temperature and density profiles near the shoulder at 60 s for various vibrational relaxation times.

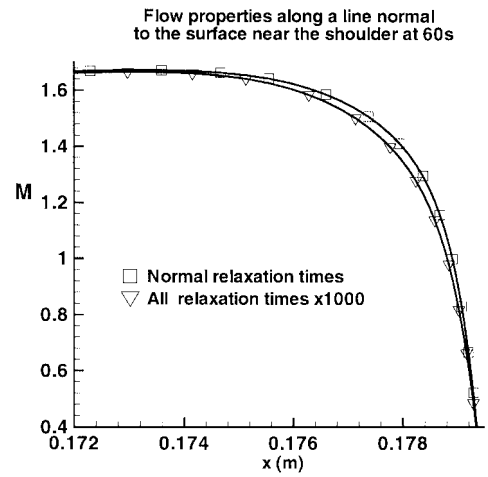

Fig. 34 Effect of vibrational nonequilibrium on Mach number profiles near the shoulder at 60 s.

In Figs. 33–37, vibrational relaxation effects on the afterbody aerothermal environment are examined. Figure 33 is a plot of the translational temperature, vibrational temperature, and density along a line normal to the surface at the shoulder for the calculations with various relaxation times at 60 s. As expected, as the vibrational relaxation times increase, the shock standoff distance increases, and the overshoot in the vibrational temperature at the shock decreases. Slight changes in the density profiles are observed in the shock region.

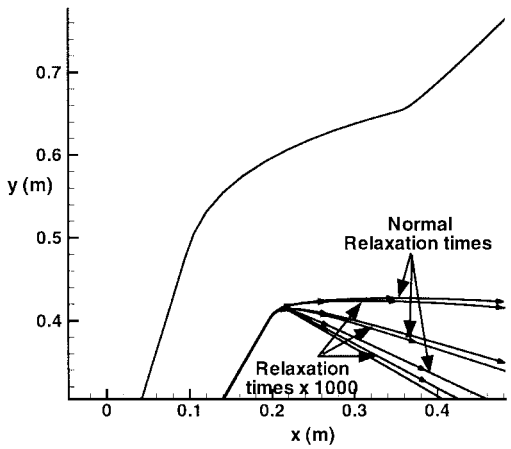

Fig. 35 Effect of vibrational nonequilibrium on the flow streamlines at 60 s.

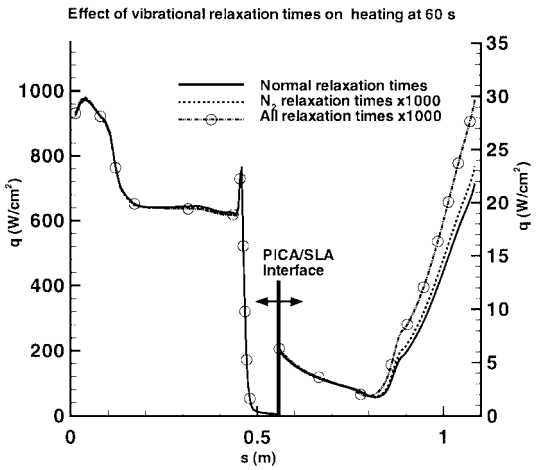

Fig. 36 Effect of vibrational nonequilibrium on the afterbody heating at 60 s.

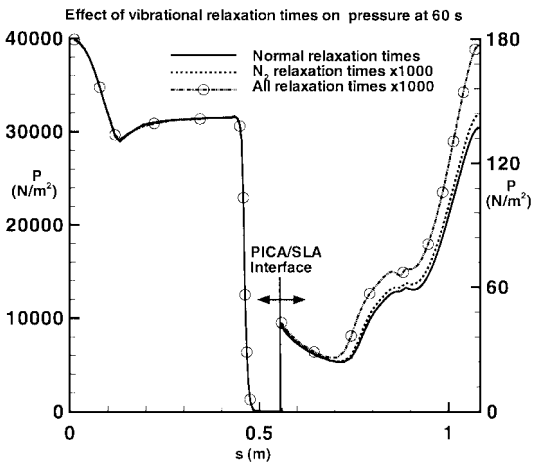

Fig. 37 Effect of vibrational nonequilibrium on the afterbody pressure at 60 s.

Figure 34 is a plot of the Mach number profiles (same location as in Fig. 33) for the normal relaxation time case and the case where all of the vibrational relaxations times are increased by 1000; the Mach number is calculated using a frozen speed of sound.[32] Near the surface, the increase in the vibrational relaxation times leads to a decrease in Mach number; although not shown in Fig. 34, the reduction in Mach number for the solution where the N_2 vibrational relaxation times are increased lies between the two curves.

Figure 35 is a plot of streamlines that pass through the forebody shoulder region and expand into the afterbody region. Three pairs of streamlines are presented; each pair consists of a streamline originating from an identical location in the forebody shoulder region for the normal vibrational relaxation solution and the all vibrational relaxation times increased solution. For the increased vibrational relaxation time case (larger shock standoff), the flow turns more toward the body than for case with the normal vibrational relaxation times; the streamlines for the case where N_2 vibrational times are increased lies between the curves for the other cases.

Figures 36 and 37 are plots of heating and pressure along the forebody and afterbody; forebody and afterbody values are shown on different scales indicated by arrows in Figs. 36 and 37. The afterbody heating and pressure increase significantly with the increase in vibrational relaxation times. The increase in heating and pressure are about 35% and 25% between the normal vibrational relaxation time solution and the all vibrational relaxation times increased solution; the N_2 vibrational relaxational time case lies between the other two solutions. On the forebody, the difference in heating and pressure distributions between the three cases as a result of the increased vibrational relaxation times is minimal. Thus, these results demonstrate that the wake flow structure and the afterbody heating and pressure profiles are altered by increasing the vibrational relaxation times. Larger vibrational relaxation times, which increase the forebody shock standoff distance, produce an increase in the afterbody pressure and heating profiles.

In Figs. 38–43, the relationship between the forebody geometry and the afterbody pressure and heating distributions is investigated.

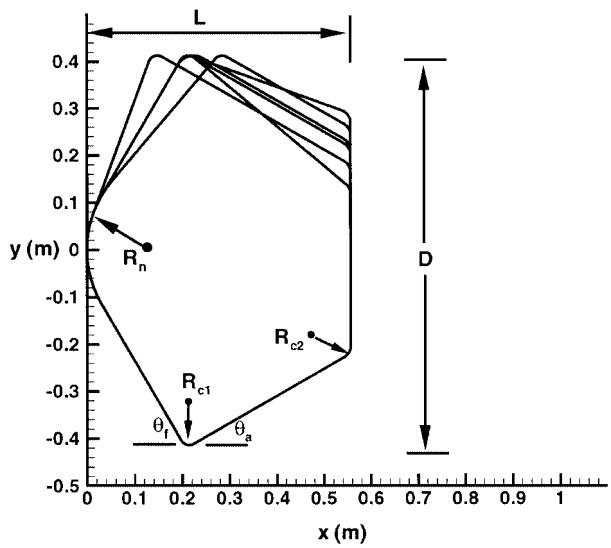

Fig. 38 Geometry parameterization and application for various geometries.

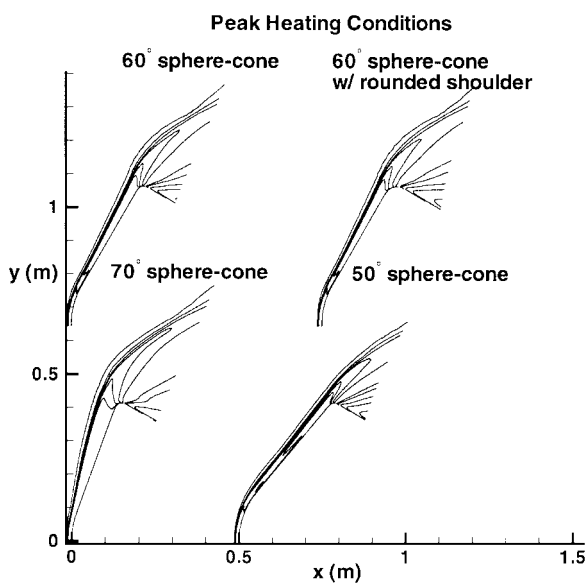

Fig. 39 Natural log of density contours near the shoulder for three SRC forebody cone angles at peak heating.

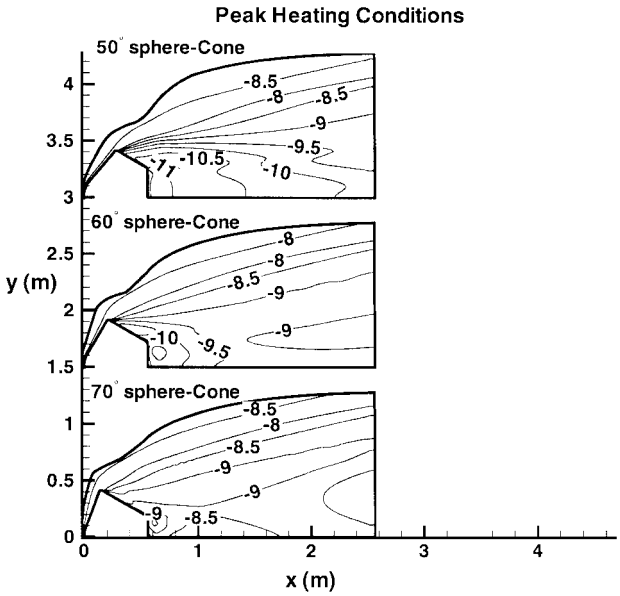

Fig. 40 Natural log of density contours in the wake for three SRC forebody cone angles at peak heating.

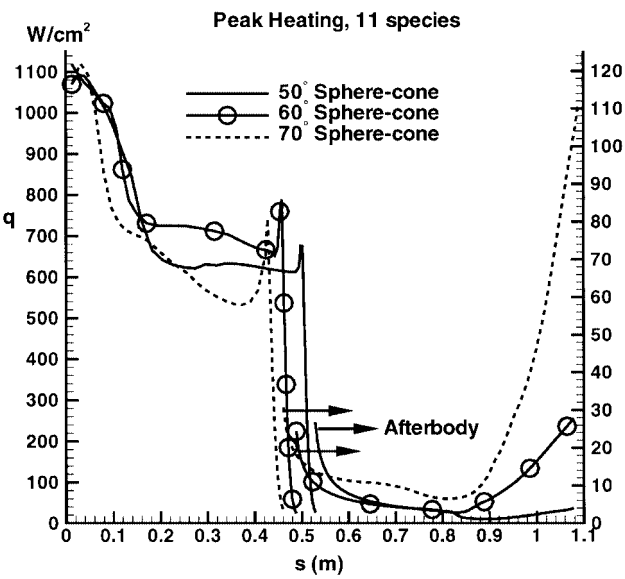

Fig. 41 Surface convective heating distributions for the various forebody cone angles at 54 s.

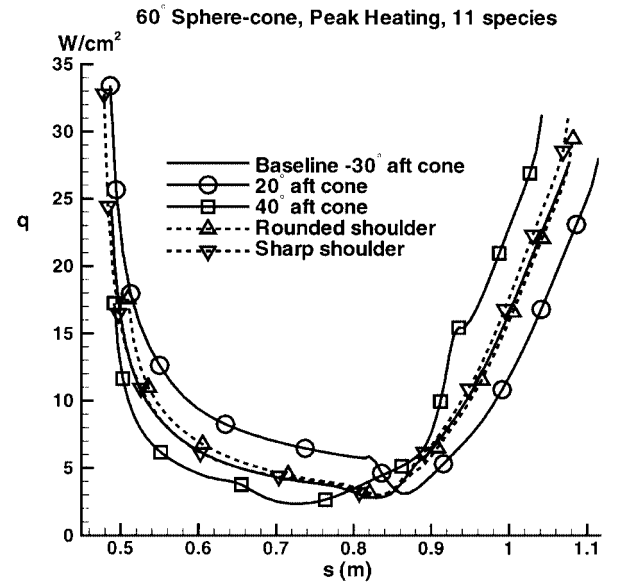

Fig. 42 Afterbody heating distributions for various geometries at 54 s.

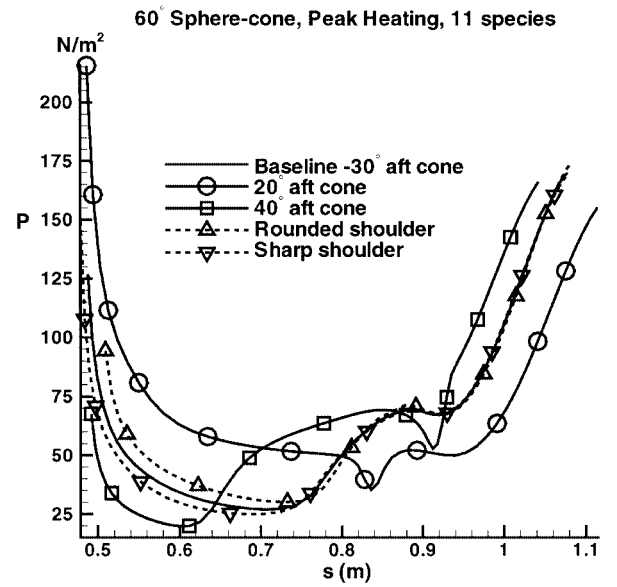

Fig. 43 Afterbody pressure distributions for various geometries at 54 s.

A number of flow solutions are generated at the peak heating conditions for seven geometries. For these cases, the vibrational relaxation times are held constant, and the forebody shock standoff distance is changed by altering the forebody geometry. The parameterization for these geometries is listed in Table 6 and plotted in Fig. 38. The length, diameter, and nose radius are held constant while forebody cone angle is increased and decreased to alter the forebody shock standoff distance. With this parameterization, the length of the afterbody conic and base radius change as the cone angle changes. Thus, to determine the effect of changing the base radius, the afterbody cone angle is varied for two cases with the forebody cone angle held constant. Finally, the shoulder corner radius is varied to determine its effects on the afterbody heating and pressure distributions.

In Figs. 39 and 40, the natural log of density contours at the shoulder and in the wake are plotted for the 50-, 60-, and 70-deg sphere–cones and the 60-deg sphere–cone with a rounded shoulder (geometries 1–3 and 6 in Table 6). In Fig. 39, the shock standoff distance at the shoulder clearly decreases as the forebody cone angle increases. In Fig. 40, in the wake, as the forebody cone angle is decreased and the shock standoff distance decreases, the density in the wake recompression region decreases. Between the 50- and 70-deg sphere–cones, the density increases by about a factor of 8 near the base of the afterbody (a smaller negative number corresponds to a larger density). Finally, for the 60-deg cone, increasing or decreasing the shoulder corner radius had a minimal effect on the flow density profiles.

In Fig. 41, surface convective heat transfer distributions are plotted for the cases where the forebody cone angle is modified. On the forebody, all of the solutions predict nearly equal stagnation heat transfer values; this result is expected because the nose radius is constant for all of the shapes. The shape of the heating profiles are similar for the 50-deg sphere–cone and the baseline 60-deg sphere–cone geometries. The 50-deg sphere–cone gives a lower heating on the frustum of the cone as a result of the smaller cone angle. However, with the diameter held constant, the smaller cone angle exposes a larger forebody surface area to the heating. For the 70-deg sphere–cone, less heating is predicted on the frustum of the cone. The shape of the profile is different because the sonic line attaches at the shoulder. For the 50- and 60-deg sphere–cones, the sonic line attaches near the sphere–cone juncture.

On the afterbody in Fig. 41, significant differences in the convective heating profiles are observed. The base heating for the 70-deg sphere–cone is greatly enhanced, whereas the base heating for the

50-deg sphere–cone is greatly reduced. The afterbody stagnation heating values are 110 W/cm^2 for the 70-deg sphere–cone, 30 W/cm^2 for the 60-deg sphere–cone, and 4 W/cm^2 for the 50-deg sphere–cone. Although not shown, similar results were obtained for the afterbody pressure profiles. The increase in heating as the cone angle increases is consistent with the wake density profiles in Fig. 40. Further, these results support the hypothesis that the afterbody heating and pressure profiles are a strong function of the forebody shock structure near the shoulder.

In Fig. 41, the ratio of afterbody stagnation convective heating to forebody stagnation heating varies from about 10% to 0.5% depending on the forebody cone angle. A typical design approach is to use a fraction of the forebody stagnation heating on the afterbody. Usually, this fraction is obtained from wind-tunnel data.[57] For example, on Apollo, a scaling value of 3% of the forebody stagnation heating was used for the afterbody heatshield design. Comparisons with the flight data showed the preflight heating calculations overpredicted the heating by a factor of two for the attached flow on the afterbody. This trend is consistent with the results in this work because the shock standoff distance in a perfect-gas hypersonic wind tunnel is larger than the real-gas flight value. It is shown that a larger forebody shock standoff distance produces higher leeside heating. Hence, for Apollo, the afterbody heating in the wind tunnel was higher than the flight data. This example and the results in this paper illustrate that both geometry and the modeling of the flow physics are important considerations for afterbody heat transfer predictions and heatshield design.

Finally, in Figs. 42 and 43, afterbody convective heating and pressure distributions are shown for the geometries (4–7 in Table 6) with the different shoulder corner radii, the different afterbody cone angles, and the baseline (1 in Table 6); for all of the shapes, the forebody is a 60-deg sphere–cone. For all of the cases, the forebody heating distributions are similar and are not shown. In Figs. 42 and 43, the heating and pressure distributions in the afterbody are minimally affected by changing the shoulder corner radius. Slightly higher and lower pressures are observed on the afterbody cone frustum from increasing or decreasing the shoulder corner radius. For a 60-deg sphere–cone, these results are reasonable because the sonic line is attached near the sphere–cone juncture. In Fig. 39, it is seen that rounding the shoulder on the 60-deg sphere–cone does not alter the density contour profiles. For a geometry with the sonic line attached at the shoulder such as 70-deg sphere–cone, more of an effect on the afterbody environment would be expected.

Decreasing the aft cone angle produces higher heat transfer and pressure on the afterbody cone frustum because the flow expansion angle is decreased. The increased base diameter reduces the amount of base heating. Increasing the aft cone angle generates the opposite trends leading to higher heat transfer on the base but less on the aft cone frustum. The pressure rise at $s = 0.6$ m for the 40-deg aft cone geometry is a result of flow separation on the afterbody conic section. For the 20- and 30-deg aft cone geometries, the flow does not separate until the end of the afterbody conic is reached.

From the geometry study, it is concluded that altering the forebody cone angle, which increases or decreases the forebody shock standoff distance, has the most influence on the afterbody heating and pressure profiles. A change in the forebody cone angle from 50 to 70 deg increased the peak afterbody base heating from 4.0 to 110.5 W/cm^2 (2662.5%). A change in the afterbody conic angle from 20 to 40 deg had a secondary effect, producing changes of only about 10% in the base heating. For a 60-deg sphere–cone, increasing or decreasing the shoulder radius had almost no effect on the afterbody heating and pressure profiles.

In summary, these results support the hypothesis that increasing the shock standoff distance in the shoulder region alters the expansion around the shoulder, which allows more mass to be ingested into the afterbody recirculation region, which increases the pressure and the heat transfer. For the 60-s entry conditions, as the vibrational relaxation times are increased, the shoulder shock moves away from the body, the Mach number near the surface decreases, and the flow turns more toward the afterbody conic as it expands around the shoulder. The increased flow turning angle leads to more mass being ingested into the afterbody recirculation region, which increases the heat transfer and the pressure on the back of the afterbody. Further, these results are consistent with the heating and pressure profiles observed on the afterbody base along the trajectory (see Figs. 22 and 23). The relative drop in heating and pressure on the afterbody base observed at the 60-s conditions is explained by vibrational overrelaxation at the forebody shoulder (see Fig. 31), which decreases the shock standoff distance. These results were also confirmed by a geometry study, which showed that the increasing or decreasing the forebody cone angle, which increases the forebody shock standoff distance, allows more or less mass to be ingested into the afterbody recirculation region, which increases or decreases the afterbody heating and pressure profiles.

Effect of Forebody Ablation on the Wake Aerothermal Environment

In this section, the effects of forebody ablation on the wake aerothermal environment are described. Forebody ablation products in the wake are potentially a source of the afterbody heating and pressure profiles generated for Stardust. For Viking, forebody ablation products were posited as an explanation for the dual pressure peaks measured in on the based of the afterbody.[23] Therefore, full-body simulations with and without forebody ablation products are compared, and the effects on the wake aerothermal environment of parametrically increasing the surface blowing rate in the forebody are examined. Further, the effects of CO catalysis on the afterbody heating are investigated; with forebody ablation, CO is a major component of the wake recirculation region. The flow simulations with forebody ablation use an 18-species chemistry model with an afterbody that is assumed to be nonablating and fully catalytic to either O, N, and ions, or CO, N, and ions. The simulations without forebody ablation use an 11-species chemistry model with an afterbody that is assumed to be nonablating and fully catalytic to O, N, and ions. Both the 18- and 11-species simulations assume the afterbody is a radiative equilibrium wall with an emissivity of 1.

Figure 44 shows CO and O mass fractions in the wake at the 48- and 66-s trajectory conditions. The calculations include the effects of CO catalysis. These points are before and after peak heating (Table 5). A significant amount of CO and O is entrained in the wake as a result of forebody ablation and dissociation of O in the shock layer. The CO mass fraction is largest near the afterbody back surface and decreases as the shear layer is approached. The O mass fraction is largest near the edge of the shear layer and decreases as the surface is approached. The gradients in the O and CO mass fractions occur because the primary source of O is from dissociation in the forebody shock layer whereas the primary source of CO is from mass injection via ablation. Thus, the O mass fraction peaks near the boundary-layer edge and diminishes as the surface is approached. The opposite trend occurs for CO. These gradients are propagated into the wake recompression region. Finally, the CO mass fraction is slightly larger at the 66-s trajectory conditions, and the O mass fraction is slightly larger at the 48-s conditions.

The forebody ablation products in the wake significantly alter the temperature distributions and the amount of vibrational nonequilibrium in the recompression region behind the SRC. The translational temperatures and the amount of vibrational nonequilibrium are much higher in the wake without ablation as compared to calculations with forebody ablation. To understand this result, a number of cases are generated at the 54-s conditions with the amount of mass injection increased or decreased. The peak heating conditions (54 s) produce the maximum mass injection rate and are used as a baseline to parametrically vary the amount of mass injection. For the cases where the blowing rate is varied, the forebody temperature and species concentrations are held constant at the baseline value. As described in the "Procedure" section, the mass injection rate, surface temperatures, and surface species concentrations are generated with fully coupled mass and energy balances that account for the forebody ablation products and the time history of the material response. As the blowing rate is increased and decreased from the baseline value, the heat transfer decreases or increases. The increase or decrease in heating alters the TPS material response, which would produce a different surface temperature distribution, species concentration distribution, and blowing rate distribution. This effect is not included in the calculations. Thus, the solutions do not reflect the actual TPS material response and are only used to qualitatively

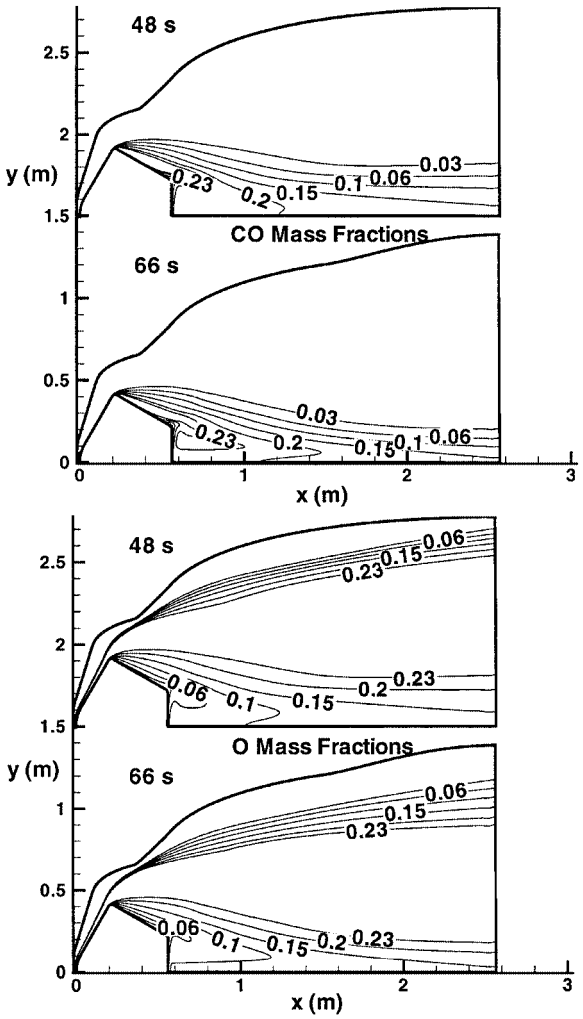

Fig. 44 CO and O mass fraction contours at 48 and 66 s.

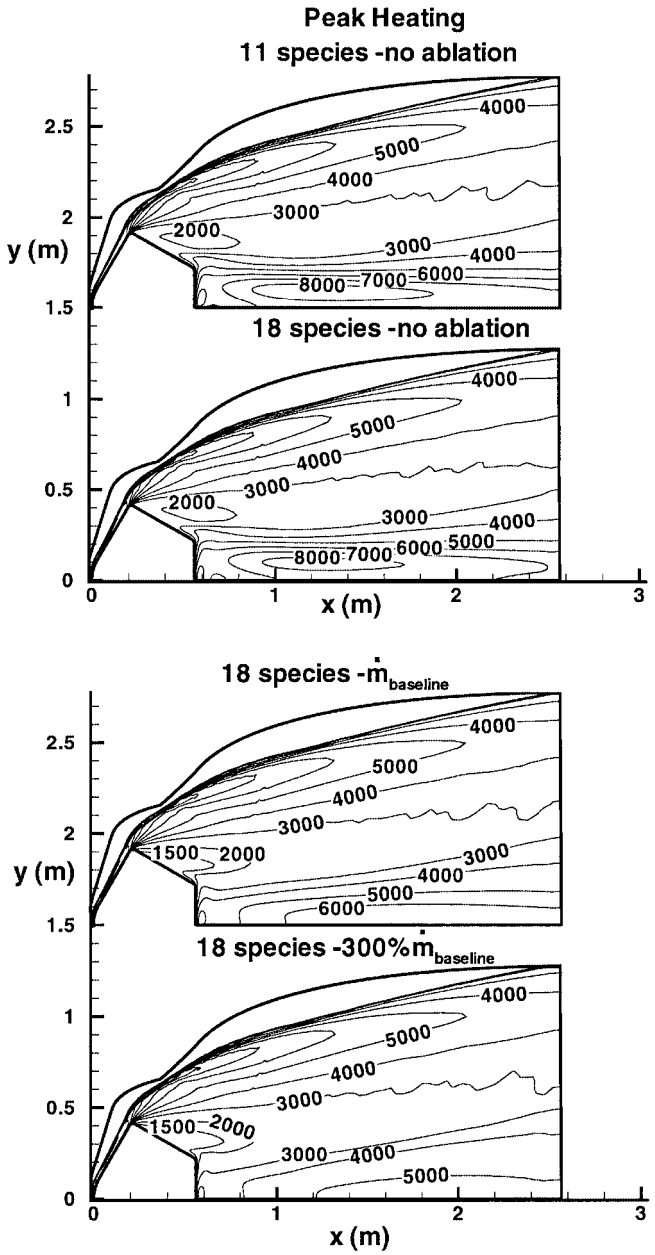

Fig. 45 Translational temperature contours at peak heating with different chemistry and ablation models.

investigate the effects of increasing or decreasing the amount of forebody ablation.

In Figs. 45 and 46, wake translational temperature contours and the ratio of the vibrational temperature to the translational temperature contours are plotted for four solutions at peak heating: 1) an 11-species chemistry model with no forebody ablation, 2) an 18-species chemistry model with no forebody ablation, 3) an 18-species chemistry model with the baseline mass injection on the forebody, and 4) an 18-species chemistry model with 300% of the baseline mass injection. The calculations without ablation exhibit much higher translational temperatures in the wake recompression region. The peak temperature without ablation is about 9000 K. With ablation, the translational temperature in the recompression region is significantly decreased. Slight differences in the translational temperature contours are observed for the nonablating 18- and 11-species cases. The wake recompression region temperatures are significantly reduced by increasing the blowing rate on the forebody.

The decrease in translational temperature in the wake with ablation is the result of vibrational relaxation promoted by CO. In Fig. 46, the amount of vibrational nonequilibrium is much greater for the nonablating flow solutions. The vibrational nonequilibrium leaves more energy in the translational modes leading to the higher temperatures. For the ablating cases, the CO from the forebody promotes translational–vibrational energy transfer, which reduces the translational temperature and promotes thermal equilibrium. Thus, adding more CO, by increasing the forebody mass injection rates, reduces the translation temperature via transfer of energy to the CO vibrational modes.

The effects of forebody ablation on the afterbody heat transfer as a function of CO catalysis and forebody mass blowing rate are shown in Figs. 47–49. Given the large CO mass fraction in the wake, CO catalysis is modeled in the nonablating afterbody boundary condition, and new flow calculations are generated along the entire trajectory. Further, flow solutions are generated at peak heating with the blowing rate parametrically varied.

In Fig. 47, the predicted convective heating at the afterbody stagnation point along the entry trajectory is compared for flow solutions with three combinations of modeling parameters: 1) 18-species chemistry, forebody ablation, and CO, N, and ion catalysis on the afterbody; 2) 18-species chemistry, forebody ablation, and O, N, and ion catalysis on the afterbody (see Fig. 23); and 3) 11-species chemistry, no forebody ablation, and O, N, and ion catalysis on the afterbody (see Fig. 23). The curves are spline fits of the predicted heating values. With CO catalysis, the maximum increase in heating is about 20%. The increase in total heatload, however, is less.

Early in the trajectory, shown in Fig. 47, although the mass fraction of CO in the wake is large (see Fig. 44), the heating is not increased as a result of CO catalysis because the rate of CO recombination is diffusion limited by the amount of available O. Later in the trajectory, when the pressure and density in the wake increase (see Fig. 22), the amount of available oxygen increases, and the effects of CO catalysis are evident. Comparing the calculations

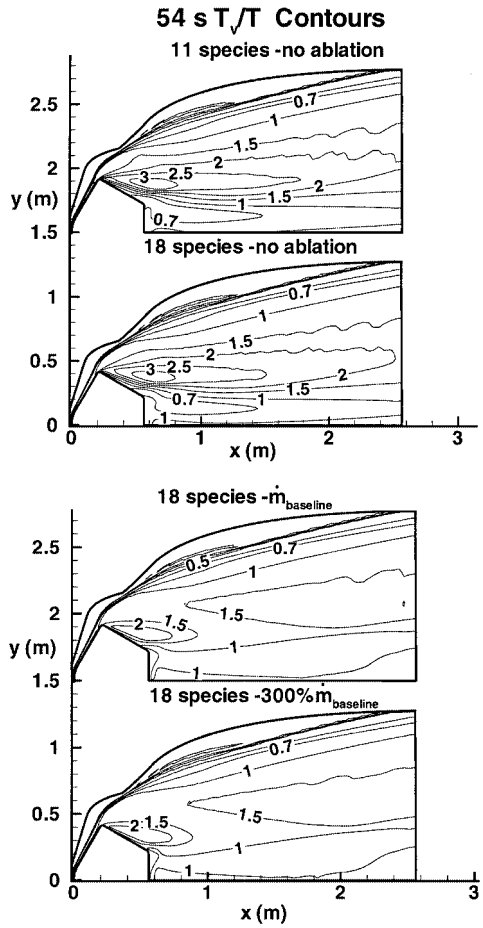

Fig. 46 Vibrational/translational temperature contours at peak heating with different chemistry and ablation models.

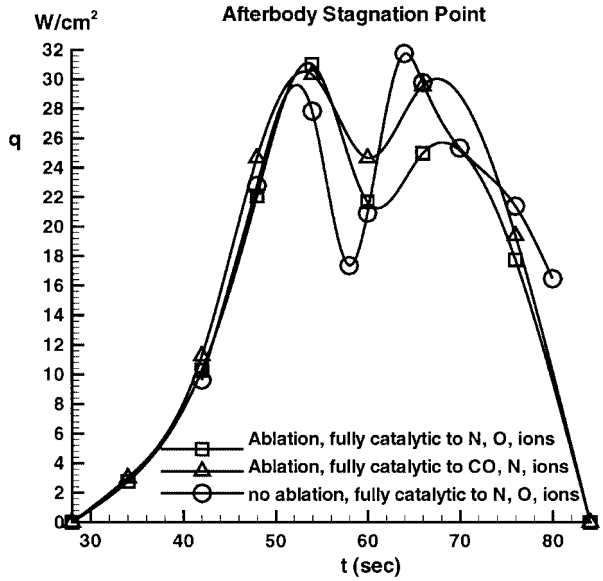

Fig. 47 Afterbody stagnation heating along the trajectory.

with forebody ablation and CO catalysis to the 11-species calculations without forebody ablation, the predictions are in fairly good agreement except at 60 s. Note, more points were generated for the 11-species calculations, which magnifies differences in the spline-fit distributions.

In Fig. 48, surface convective heating predictions are compared for five nonablating and ablating flow solutions at peak heating: 1) 18-species chemistry, baseline forebody ablation, and CO, N, and ion catalysis on the afterbody; 2) 18-species chemistry, 200% forebody ablation, and CO, N, and ion catalysis on the afterbody;

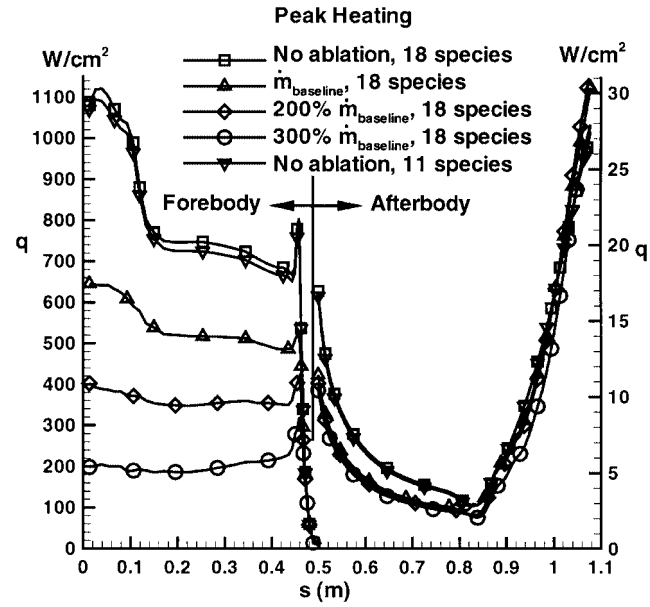

Fig. 48 Surface heating distributions as a function of blowing rate at 54 s.

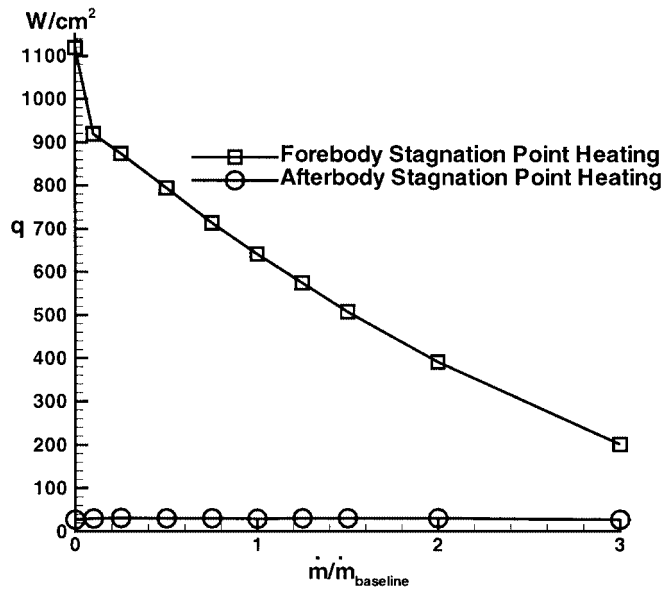

Fig. 49 Forebody stagnation heating and afterbody stagnation heating as a function of blowing rate at 54 s.

3) 18-species chemistry, 300% forebody ablation, and CO, N, and ion catalysis on the afterbody; 4) 18-species chemistry, no forebody ablation, and O, N, and ion catalysis on the afterbody; and 5) 11-species chemistry, no forebody ablation, and O, N, and ion catalysis on the afterbody. On the forebody, the surface heat transfer rapidly decreases as the mass injection rate is increased. On the afterbody, the heat transfer on the frustum of the cone is slightly higher for the nonablating calculations, but the results are all similar on the base of the SRC. The nonablating 18-species and 11-species calculations produced very similar heat transfer distributions on the forebody and afterbody. The afterbody heat transfer rate was relatively unaffected by doubling or tripling the blowing rate in the forebody. This trend results from the CO catalysis being diffusion limited by the amount of available oxygen.

In Fig. 49, the forebody and the afterbody stagnation convective heat transfer is plotted as a function of the mass injection rate divided by the baseline mass injection rate; a value of zero is the nonablating result. The calculations use an 18-species chemistry model, and the ablating cases include CO catalysis. On the forebody, the stagnation heat transfer is fairly linear with increases or decreases in the mass injection rate. On the afterbody, the base heat transfer remains

constant as a function of mass injection rate. The heating is not affected by increases or decreases in the amount of CO. This supports the earlier conclusion that the CO surface catalysis in the wake is limited by O diffusion.

In summary, forebody ablation effects were investigated on the wake aerothermal environment. It was shown that the forebody ablation products significantly change the afterbody temperature and mass fraction distributions in the wake recompression region. CO from the forebody ablation products absorbs vibrational energy, thus reducing the translational temperature and the amount of vibrational nonequilibrium as compared to a nonablating calculation. CO catalysis on the afterbody increases the convective heat transfer late in the trajectory as compared to O catalysis. Early in the trajectory, the CO catalysis is diffusion limited by available O, and the differences between the calculations with and without ablation are small. At peak heating conditions, large variations in the forebody mass blowing rate had a minimal affect on the afterbody heat transfer distributions. From these results, it is concluded that for laminar wake flow that the influence of the forebody ablation products on the afterbody heating is a secondary effect when compared to the influence of forebody geometry described in the preceding section. Also, it is concluded that the bimodal heat transfer and pressure distributions on the afterbody are a result of changes in the shock standoff distance from vibrational relaxation near the forebody shoulder and not from forebody ablation products.

Conclusion

The development of a high-fidelity methodology for predicting entry flows with coupled radiation ablation was described. The prediction methodology consists of an axisymmetric, nonequilibrium, Navier–Stokes flow solver (GIANTS) loosely coupled to radiation (NOVAR) and material thermal response (FIAT) modules. The methodology was used to simulate the entry of the Stardust SRC and to generate an extensive aerothermal design database. Specifically, the aerothermal calculations were used to size the PICA forebody and SLA-561V afterbody heatshields and to develop arcjet test conditions and models for all of the major SRC heatshield components. The results demonstrate that high-fidelity flow simulations with radiation and ablation can be used as an integral part of the heatshield design process.

Flow calculations with and without ablation were generated and compared; the nonablating solutions were used for developing arcjet test conditions and models whereas the ablating flow solutions were used to size the TPS. For the forebody, surface ablation reduced the surface heat transfer, temperature, and shear, but did not affect the pressure. At peak heating, the reduction in heating from ablation was about 35%; after peak heating, where the blowing rate is less, the reduction in heating from ablation was lower. The reduction in heating from ablation resulted primarily from reduced diffusive heating.

For the forebody heatshield, the integrated heat load, TPS thickness, and recession were calculated. The maximum integrated heatload was about 28,000 J/cm^2 with the radiative component about 7% of the total. The maximum calculated TPS thickness was about 4.8 cm; this value with margin was used directly to design the forebody heatshield. The maximum predicted surface recession rate was about 1.2 cm at the stagnation point. The predicted shape as a result of surface recession was used in the aerodynamic calculations.

For the afterbody, sufficient high-fidelity wake flow solutions were calculated along the trajectory to define the afterbody heating and pressure distributions in time. A number of important observations were made. First, the forebody and the afterbody pressure and heating distributions in time were different. By the comparing of the forebody and afterbody stagnation regions, it was found that the heat pulse on the afterbody is longer than on the forebody, and the peaks in pressure and heat transfer on the afterbody occur later in the trajectory than on the forebody. Finally, the shape of profiles were distinctly different. The forebody heating and pressure profiles are parabolic whereas the afterbody base pressure and heating profiles display a bimodal shape. When applied to the afterbody TPS, these results show that the traditional afterbody heatshield design approach is nonconservative for the Stardust SRC shape and entry conditions.

The distinct shape and characteristics of the afterbody heating and pressure distributions are theorized to be a function of the flow expansion around the shoulder. As the forebody shock moves away from shoulder, more mass is ingested into the afterbody conic boundary layer, which is then recompressed in the afterbody base region producing higher pressures and heating. This theory explains most of the differences between the forebody and afterbody pressure and heating distributions in time observed in this work. Also, afterbody pressure and heating data from Viking, Mars Pathfinder, and Apollo are consistent with this theory. This theory was confirmed and tested in two ways: 1) changing the vibrational relaxation times and 2) altering the SRC geometry.

By varying the vibrational relaxation times to adjust the forebody shock standoff distance, it was found that increasing the vibrational relaxation times and, hence, the forebody shock standoff distance produces higher heating on the base of the afterbody. Thus, the bimodal afterbody pressure and heating distributions are explained by vibrational overrelaxation after peak heating. The increased vibrational relaxation decreases the forebody shock standoff distance at the shoulder, which leads to a reduction in the heating and pressure on the base of the SRC.

By varying the forebody cone angle, it was found that the afterbody heating and pressure profiles and the amount of mass in the wake recirculation region significantly increased or decreased as the cone angle increased or decreased; the forebody shock standoff distance increases or decreases as the cone angle increases or decreases. Also, flow solutions were generated where the shoulder corner radius, afterbody cone angle, and the mass blowing rate in the forebody were varied. These modifications altered the afterbody heating and pressure distributions, but were a secondary effect relative to changes in the forebody cone angle.

Acknowledgments

The work of the second and third authors is supported by the Reacting Flow Environments branch of NASA Ames Research Center through Contract NAS2-14031 to Eloret; this support is gratefully acknowledged. The authors would like to thank Carol Davies (NASA Ames Research Center/Reacting Flow Environments Branch) for support; Huy Tran [NASA Ames Research Center/Thermal Protection Materials and Systems Branch (ASM)], Christine Johnson (NASA Ames Research Center/ASM), and Harry Dill (NASA Ames Research Center/Space Projects Division) for materials and project support; members of the Lockheed Martin Denver aerothermal team, C. Thomas Edquist, W. H. Wilcockson, Roger Giellis, Jan Thorton, and C. Deats, for the Stardust SRC design support; and Robert A. Mitcheltree (NASA Langley Research Center/Aerothermodynamics Branch) and P. Desai (NASA Langley Research Center/Vehicle Analysis Branch) for helpful discussions regarding the SRC aerodynamics and stability and its relation to the heating environment.

References

[1] Wilcockson, W. H., "Stardust Sample Return Capsule Design Experience," AIAA Paper 98-2854, June 1998.

[2] Kawaguchi, J., Fujiwara, A., and Sawai, S., "Sample and Return Mission from Asteroid Nereus via Solar Electric Propulsion," *Acta Astronautica*, Vol. 38, No. 2, 1996, pp. 87–101.

[3] Matousek, S., Adler, M., and Lee, W., "A Few Good Rocks: The Mars Sample Return Mission Architecture," AIAA Paper 98-4282, Aug. 1998.

[4] Tran, H. K., Johnson, C., Hsu, M.-T., Smith, M., Dill, H., and Chen-Johnson, A., "Qualification of the Forebody Heatshield of the Stardust's Sample Return Capsule," AIAA Paper 97-2482, June 1997.

[5] Johnson, C. E., Tran, H. K., Smith, M., Dill, H., and Etienne, L., "Stardust Backshell and Back Interface Plate Design Verification Tests in the NASA Ames Arc Jet Facilities," AIAA Paper 97-2483, June 1997.

[6] Mitcheltree, R. A., Wilmoth, R. G., Cheatwood, F. M., Braunckmann, G. J., and Greene, F. A., "Aerodynamics of Stardust Sample Return Capsule," AIAA Paper 97-2304, June 1997.

[7] Desai, P. N., Mitcheltree, R. A., and Cheatwood, F. M., "Entry Dispersion Analysis for the Stardust Sample Return Capsule," AIAA Paper 97-3812, Aug. 1997.

[8] Tran, H., Johnson, C., Rasky, D., Hui, F., Chen, Y.-K., and Hsu, M., "Phenolic Impregnated Carbon Ablators (PICA) for Discovery Class Mission,"

AIAA Paper 96-1911, June 1996.

[9]Olynick, D. R., Henline, W. D., Chamber, L. H., and Candler, G. V., "Comparisons of Coupled Radiative Flow Solutions with Project Fire II Flight Data," *Journal of Thermophysics and Heat Transfer*, Vol. 9, No. 4, 1995, pp. 586–594.

[10]Chen, Y.-K., and Milos, F. S., "Ablation and Thermal Response Program for Spacecraft Heatshield Analysis," AIAA Paper 98-0273, Jan. 1998.

[11]Olynick, D., Chen, Y.-K., and, Tauber, M., "Forebody TPS Sizing with Radiation and Ablation for the Stardust Sample Return Capsule," AIAA Paper 97-2474, June 1997.

[12]Olynick, D., Chen, Y.-K., and Tauber, M., "Wake Flow Calculations with Radiation and Ablation for the Stardust Sample Return Capsule," AIAA Paper 97-2477, June 1997.

[13]Olynick, D., "Aerothermodynamics of the Stardust Sample Return Capsule," AIAA Paper 98-0167, Jan. 1998.

[14]Cornette, E. S., "Forebody Temperatures and Calorimeter Heating Rates Measured During Project Fire II Reentry at 11.35 km/s," NASA TM X-1305, Nov. 1966.

[15]Chen, Y.-K., Henline, W. D., and Tauber, M. E., "Trajectory Based Heating and Ablation Calculations for Mars/Pathfinder Aeroshell," *Journal of Spacecraft and Rockets*, Vol. 32, No. 2, 1995, pp. 225–230.

[16]"User's Manual Aerotherm Charring Material Thermal Response and Ablation Program: CMA87," Acurex Corp., Rept. UM-87-11/ATD, Mountain View, CA, Aug. 1987.

[17]Bhutta, B. A., Daywitt, J. E., Rahaim, J. J., and Brant, D. N., "A New Technique for the Computation of Severe Reentry Environments," AIAA Paper 96-1861, June 1996.

[18]Gupta, R. N., Kam-Pui, L., Moss, J. N., and Sutton, K., "Viscous-Shock-Layer Solutions with Coupled Radiation and Ablation Injection for Earth Entry," AIAA Paper 90-1697, June 1990.

[19]Henline, W. D., and Tauber, M. E., "Trajectory-Based Heating Analysis for the European Space Agency/Rosetta Earth Return Vehicle," *Journal of Spacecraft and Rockets*, Vol. 31, No. 3, 1994, pp. 421–428.

[20]Wilson, K. H., "Stagnation Point Analysis of Coupled Viscous-Radiating Flow with Massive Blowing," NASA CR-1548, June 1970.

[21]Mitcheltree, R. A., and Gnoffo, P. A., "Wake Flow About a MESUR Mars Entry Vehicle," AIAA Paper 94-1958, June 1994.

[22]Haas, B. L., and Venkatapathy, E., "Mars Pathfinder Computations Including Base-Heating Predictions," AIAA Paper 95-2086, June 1995.

[23]"Entry Data Analysis for Vikings 1 and 2: Final Report," Martin–Marietta, TN-3770218, Denver, CO, Nov. 1976.

[24]Milos, F. S., Chen, Y.-K., Congdon, W. M., and Thornton, J. M., "Mars Pathfinder Entry Temperature Data, Aerothermal Heating, and Heatshield Material Response," AIAA Paper 98-2681, June 1998.

[25]Lee, D. B., and Goodrich, W. D., "The Aerothermodynamic Environment for the Apollo Command Module During Superorbital Entry," NASA TN D-6792, April 1972.

[26]Hollis, R. B., and Perkins, J. N., "Hypervelocity Heat-Transfer Measurements in an Expansion Tube," AIAA Paper 96-2240, June 1996.

[27]Hollis, R. B., and Perkins, J. N., "Comparison of Experimental and Computational Aerothermodynamics of a 70-deg Sphere-Cone," AIAA Paper 96-2240, June 1996.

[28]Gnoffo, P. A., "A Code Calibration Program in Support of the Aeroassist Flight Experiment," AIAA Paper 89-1673, June 1989.

[29]Gnoffo, P. A., Gupta, R. N., and Shinn, J. L., "Conservation Equations and Physical Models for Hypersonic Air Flows in Thermal and Chemical Nonequilibrium," NASA TP-2867, Feb. 1989.

[30]Park, C., *Nonequilibrium Hypersonic Aerothermodynamics*, Wiley, New York, 1990, pp. 324–327.

[31]Lee, J.-H., "Basic Governing Equations for the Flight Regimes of Aeroassisted Orbital Transfer Vehicles," *Thermal Design of Aeroassisted Orbital Transfer Vehicles*, edited by H. F. Nelson, Vol. 96, Progress in Astronautics and Aeronautics, AIAA, New York, 1985, pp. 3–53.

[32]Candler, G. V., "The Computation of Weakly Ionized Hypersonic Flows in Chemical Nonequilibrium," Ph.D. Dissertation, Dept. of Aeronautics and Astronautics, Stanford Univ., Stanford, CA, June 1988.

[33]Candler, G. V., and MacCormack, R. W., "The Computation of Hypersonic Ionized Flows in Chemical and Thermal Nonequilibrium," *Journal of Thermophysics and Heat Transfer*, Vol. 5, No. 3, 1991, pp. 266–273.

[34]Olynick, D. R., Henline, W. D., Chambers, L. H., and Candler, G. V., "Comparisons of Coupled Radiative Navier–Stokes Flow Solutions with the Project Fire II Flight Data," AIAA Paper 94-1955, June 1994.

[35]Wilke, C. R., "A Viscosity Equation for Gas Mixtures," *Journal of Chemical Physics*, Vol. 18, No. 4, 1950, p. 517.

[36]Blottner, F. G., Johnson, M., and Ellis, M., "Chemically Reacting Viscous Flow Program for Multi-Component Gas Mixtures," Sandia Lab., Rept. SC-RR-70-754, Albuquerque, NM, Dec. 1971.

[37]Candler, G., "Computation of Thermo-Chemical Nonequilibrium Martian Atmospheric Entry Flows," AIAA Paper 90-1965, June 1990.

[38]Bartlett, E. P., Kendal, R. M., and Rindal, R. A., "An Analysis of the Coupled Chemically Reacting Boundary Layer and Charring Ablator: Part IV—A Unified Approximation for Mixture Transport Properties for Multicomponent Boundary-Layer Applications," NASA CR-1063, June 1968.

[39]Riabov, V. V., "Approximate Calculation of Transport Coefficients of Earth and Mars Atmospheric Dissociating Gases," *Journal of Thermophysics and Heat Transfer*, Vol. 10, No. 2, 1996, pp. 209–216.

[40]Desmeuzes, C., Duffa, G., and Dubroca, B., "Different Levels of Modelization for Diffusion Phenomena in Neutral and Ionized Mixtures," AIAA Paper 94-2412, June 1994.

[41]Gupta, R. N., Yos, J. M., Thompson, R. A., and Lee, K., "A Review of Reaction Rates and Thermodynamic and Transport Properties for an 11-Species Air Model for Chemical and Thermal Nonequilibrium Calculations to 30,000 K," NASA Reference Publication 1232, Aug. 1990.

[42]Park, C., "Review of Chemical-Kinetic Problems of Problems of Future NASA Missions, II: Mars Entries," *Journal of Thermophysics and Heat Transfer*, Vol. 8, No. 1, 1994, pp. 9–23.

[43]Bhutta, B. A., and Lewis, C. H., "A New Technique for Low-to-High Altitude Predictions of Ablative Hypersonic Flowfields," *Journal of Spacecraft and Rockets*, Vol. 29, No. 1, 1992, pp. 35–50.

[44]Sangisvanni, J. J., and Barber, T. J., "Role of Hydrogen/Air Chemistry in Nozzle Performances for Hypersonic Propulsion System," *Journal of Propulsion and Power*, Vol. 9, No. 1, 1993, pp. 178–183.

[45]Heicklen, J., "Gas-Phase Chemistry of Reentry," *AIAA Journal*, Vol. 5, No. 1, 1967, pp. 4–15.

[46]Wilson, J., "Ionization Rates of Air Behind High Speed Shock Waves," *Physics of Fluids*, Vol. 9, No. 10, 1966, pp. 1913–1921.

[47]Millikan, R. C., and White, D. R., "Systematics of Vibrational Relaxation," *Journal of Chemical Physics*, Vol. 39, No. 12, 1963, pp. 3209–3213.

[48]Camac, M., "CO_2 Relaxation Processes in Shock Waves," *Fundamental Phenomena in Hypersonic Flow*, edited by J. G. Hall, Cornell Univ. Press, Ithaca, NY, 1966, pp. 195–215.

[49]Huber, K. P., and Herzberg, G., *Molecular Spectra and Molecular Structure, IV: Constants of Diatomic Molecules*, D. Van Nostrand, New York, 1979, pp. 501–582.

[50]Shimanouchi, T., "Tables of Molecular Vibrational Frequencies: Consolidated Vol. 1," U.S. Dept. of Commerce, NSRDS-NBS 39, National Bureau of Standards, Washington, DC, 1983.

[51]Chambers, L. H., "Predicting Radiative Heat Transfer in Thermochemical Nonequilibrium Flow Fields: Theory and User's Manual for the LORAN Code," NASA TM-4564, Sept. 1994.

[52]Mitcheltree, R. A., and Gnoffo, P. A., "Wake Flow About the Mars Pathfinder Mars Entry Vehicle," *Journal of Spacecraft and Rockets*, Vol. 32, No. 5, 1995, pp. 771–776.

[53]Milos, F. S., and Chen, Y.-K., "Comprehensive Model for Multicomponent Ablation Thermochemistry," AIAA Paper 97-0141, Jan. 1997.

[54]Kontinos, D. A., "Coupled Thermal Analysis Method with Application to Metallic Thermal Protection Panels," *Journal of Thermophysics and Heat Transfer*, Vol. 11, No. 2, 1997, pp. 173–181.

[55]Gnoffo, P. A., Weilmuenster, K. J., Hamilton, H. H., II, Olynick, D. R., and Venkatapathy, E., "Computational Aerothermodynamic Design Issues for Hypersonic Vehicles," AIAA Paper 97-2473, June 1997.

[56]Hollis, B. R., "Experimental and Computational Aerothermodynamics of a Mars Entry Vehicle," NASA CR-201633, Dec. 1996.

[57]Lee, D. B., Bertin, J. J., and Goodrich, W. D., "Heat Transfer Rate and Pressure Measurements Obtained During the Apollo Orbital Entries," NASA TN-D 6028, Oct. 1970.

R. D. Braun
Guest Editor